Development of a myocardial perfusion phantom

G.J. (Gijs) de Vries

MSc Report

Committee:
prof.dr.ir. C.H. Slump
M.E. Kamphuis, MSc
prof.dr.ir. R.H.J.A. Slart

July 2019

023RAM2019
Robotics and Mechatronics
EE-Math-CS
University of Twente
P.O. Box 217
7500 AE Enschede
The Netherlands

Development of a myocardial perfusion phantom

G.J. (Gijs) de Vries

Wednesday 10th July, 2019

This document is designed to be read as a book, with two pages next to each other.

Abstract

In the Netherlands, the mortality rate of Coronary Vascular Disease (CVD) is on a declining trend since 1980; 69% for men and 59% for woman. Nevertheless, 272,234 men and women have been admitted for CVD related diseases in 2016, in the Netherlands, alone. 31% (84,912) had to be admitted for a full day, of which 37% specifically for ischemia. The cause of these admissions can be prevented by a timely diagnosis of possible CVD, especially in high-risk groups (obese, smokers, diabetic, physical inactive).

Myocardial Perfusion Imaging (MPI), or, simply put, the imaging of a tracer (or contrast agent) in the blood, flowing through the heart muscle, plays an important role in diagnosing heart failure and detecting Coronary Artery Disease (CAD). Imaging systems like CT, MRI, PET, or SPECT can visualise such (radioactive) tracer (or contrast agent) in the coronary arteries and in myocardial tissue. The flow of the tracer (or contrast agent) can give an indication of narrowed or blocked blood vessels.

Clinical software is biased towards the shape of the heart and thus require anatomical landmarks. Several previously developed phantoms show interesting characteristics but none are directly compatible with clinical software. Therefore, a new myocardial perfusion phantom, specifically designed for the D-SPECT, has been developed that is directly compatible with clinical software.

The phantom, described in this thesis, is unique as it is the first phantom that is directly compatible with clinical software. Its design resembles a simplified heart, consisting of a centralised cylinder, the left ventricle, with a surrounding myocardium, split into three equal, modular, chambers corresponding to the areas perfused by the three coronary arteries. The primary flow (constant, not pulsatile), i.e. the cardiac output, is generated by a pump whereas the myocardial flow is indirectly regulated by means of flow regulators.

However, in its current state, the phantom, and its set-up, cannot yet be used to validate the D-SPECT or other modalities. The phantom does not trap the tracer in the myocardium, i.e. a true 2-compartment model, and the measurements, taken with our control module, had a low Signal-to-Noise Ratio.

With further development, the myocardial perfusion phantom, as described in this thesis, can be the corner stone for future Myocardial Perfusion phantom validation studies. Not only for the D-SPECTS quantitative perfusion measurements, but also, potentially, for other modalities.

Preface

This report is the master's thesis of G.J. (Gijs) de Vries, BSc on the development of a myocardial perfusion phantom. The thesis is carried out in the form of a project. The project started on Monday 3^{rd} December 2018, and concludes on 18^{th} July 2019. The project is carried out under the chair of Robotics and Mechatronics (RAM) of the University of Twente. It is supervised by prof.dr.ir. C.H. (Kees) Slump. Daily supervision is carried out by M.E. (Marije) Kamphuis, MSc. In addition, prof.dr. R.H.J.A. (Riemer) Slart is part of the assessment committee as an external member.

Acknowledgements

I would like to start by thanking Marije Kamphuis and Kees Slump for their supervision during this project, Riemer Slart for his additional insight, and Henny Kuipers and Sander Smits for their technical support in the development phase.

Additionally, I would like to thank Jacqueline and Marloes for their help before, during, and after the experiments at the ZGT (Ziekenhuisgroep Twente), Hengelo, and all others that were involved in organising and arranging these experiments.

G.J. (Gijs) de Vries
Enschede, Wednesday 10^{th} July, 2019

Glossary

- **Anger camera:** is an analogue gamma camera, also known as a scintillation camera, that captures gamma radiation emitted by radioisotopes by means of scintillation.
- **Atherosclerosis:** is a type of Coronary Artery Disease (CAD) in which an artery is narrowed due to plaque deposits on the artery wall.
- **Incandescence:** is the emission of visible light caused by a body's high temperature.
- **Ischemia:** is a local deficiency of the blood supply to an organ (or muscle), by, for example, atherosclerosis, causing a shortage of oxygen resulting in tissue death.
- **Luminescence:** is the emission of light not resulting from incandescence.
- **Perfusion Phantom:** is a physical object that is designed to mimic the perfusion (i.e. blood flow) in a specific organ in order to evaluate, analyse, and tune the performance of imaging devices.
- **Scintillation:** emission a flash of light when excited by ionizing radiation, e.g. gamma radiation.
- **two-compartment model:** models the tracer such that exits the main flow path, i.e. a blood vessel, and interchanges tracer with surrounding tissue (or tissue mimicking material).

Abbreviations

- **AIF:** Arterial Input Function, is a reference curve, extracted from the left ventricle or left atrium, that is important in flow quantification. Intrinsic perfusion dynamics may be lost if an AIF is not extracted.
- **CAD:** Coronary Artery Disease, are diseases that reduce the blood flow to the heart which can lead to cardiac attack or cardiac arrest.
- **CT:** Computed Tomography, uses X-Ray equipment to produce tomographic images of the person (or object) which provides the user an inside view without opening that person (or object).
- **CVD:** Cardiovascular Disease, includes CAD, encompasses diseases that involve the heart and blood vessels.
- **CZT:** Cadmium Zinc Telluride, is a semiconductor that converts X-Ray (or gamma photons) into electrons. Characteristic for CZT is that it can operate in direct-conversion mode at room temperature.
- **FOV:** Field Of View, the area that is imaged by an imaging system, e.g. an ordinary photo camera.
- **GUI:** Graphical User Interface, (in this project) is a software program, on a laptop, that allows the user to set system parameters, monitor system variables, and to start/stop the flow set-up.
- **HLA:** Horizontal Long Axis cross-sectional slice, see figure 1.
- **MPI:** Myocardial Perfusion Imaging, is a procedure that allows medical professionals to evaluate the perfusion (i.e. blood flow) in the heart.
- **MRI:** Magnetic Resonance Imaging, uses magnetic fields and radio waves, rather than radiation, to create tomographic images of a person (or object).
- **PET:** Positron Emission Tomography, is an imaging technique to visualise metabolic processes in the body using radioactive tracers.

- **PMT:** Photomultiplier Tube, is a tube that multiplies electrons emitted by the photoelectric effect when photons hit the photo cathode. Combined with a scintillator, one obtains an Anger camera.
- **PWM:** Pulse-Width Modulation, is a modulation technique to reduce the average power to a system, effectively "lowering the voltage" to, for example, a pump or motor.
- **ROI:** Region of Interest, a priority area where a high density of important information is expected to reside. Typically used to focus on a particular area, ignoring the surroundings, to improve data reliability.
- **SA:** Short-Axis cross-sectional slice, see figure 1.
- **SPECT:** Single-Photon Emission Computed Tomography, is an imaging technique, using a gamma-emitting radioisotope, to generate tomographic images of the person (or object).
- **TAC:** Time-Activity Curve, is a curve with time on the X-axis and the radioactivity, decays per second, on the Y-axis. Typically, the curves are based on the radioactivity in a fixed ROI.
- **VLA:** Vertical Long Axis cross-sectional slice, see figure 1.

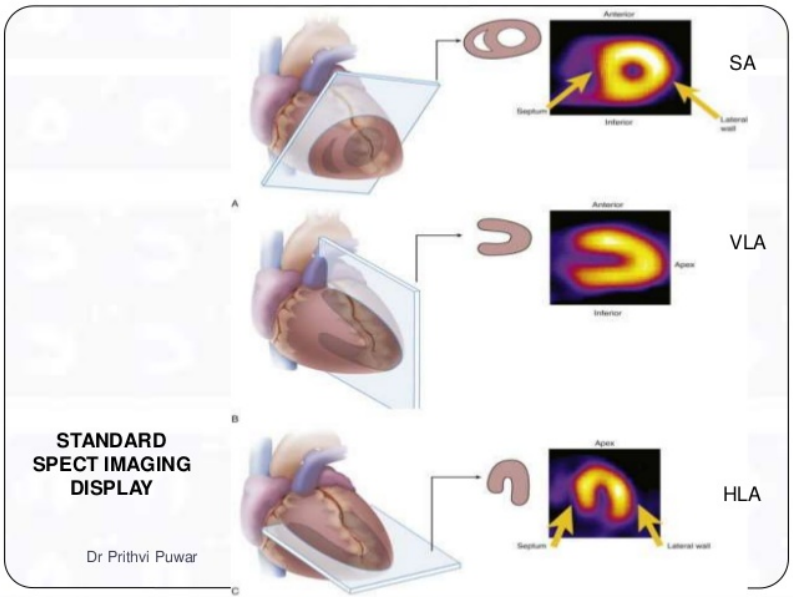

Figure 1: The SA, VLA, and HLA cross-sectional slices of the heart as they are used in the remainder of the thesis.

Contents

1 Introduction

This chapter introduces the context and the problem, from which the project is established. The chapter continues with specifying the goal, the primary requirements, and the boundaries. The last part of the chapter describes the approach and a general concept, and ends by providing an overview of the remaining thesis.

1.1 Context

In the Netherlands, the mortality rate of Coronary Vascular Disease (CVD) is on a declining trend since 1980; 69% for men and 59% for woman. Nevertheless, 272,234 men and women have been admitted for CVD related diseases in 2016, in the Netherlands, alone. 31% (84,912) had to be admitted for a full day, of which 37% specifically for ischemia (Vaartjes et al., 2013). The cause of these admissions can be prevented by a timely diagnosis of possible CVD, especially in high-risk groups (obese, smokers, diabetic, physical inactivity (Mehta et al., 2015; Mendis et al., 2011)).

Myocardial Perfusion Imaging (MPI), or, simply put, the imaging of a tracer (or contrast agent) in the blood, flowing through the heart muscle, plays an important role in diagnosing heart failure or detecting CVD, including Coronary Artery Disease (CAD). Imaging systems like CT, MRI, PET, or SPECT can visualise such (radioactive) tracer (or contrast agent) in the coronary arteries and in myocardial tissue. The flow of the tracer (or contrast agent) can give an indication of narrowed or blocked blood vessels.

Each of the four modalities, CT, MRI, PET, and SPECT, have their own strengths and weaknesses. CT uses a stable, non-radioactive, contrast agent to visualise blood flow, and has superior spatial and temporal resolution (Pelgrim et al., 2016; Khalil et al., 2011). However, CT imposes a significant radiation burden; it requires a constant bombardment of X-Rays. The superior spatial and temporal resolution allows CT to perform dynamic perfusion studies, allowing for quantitative measurements, and in turn allow for more objective diagnoses. PET and SPECT use a decaying tracer to image the blood flow, which also introduces a certain radiation burden. These tracers stay in the body until it is excreted, via urine or faeces, or until it is rendered harmless due to its natural decay over time. PET tracers typically have a much lower half-life than SPECT tracers. A short half-life complicates the procedure between the creation of the tracer and the perfusion scan. The radiation burden for both PET and SPECT, is typically lower than for CT, but comes at the cost of spatial and temporal resolution. Alternatively, MRI does not rely on any form of ionising radiation, but its low temporal resolution makes it less suitable for dynamic imaging.

Overall, SPECT is less expensive than PET, both the modality and the tracer, and is therefore more widely used for coronary and myocardial perfusion imaging. PET is more widely used in oncology due to specific PET tracer characteristics; cancerous tumours absorb the PET tracer. The less expensive SPECT does come at an alternate cost: a lower contrast and spatial resolution. However, the longer half-life of SPECT tracers make it more practical than PET tracers. Numerous developments in imaging systems, detectors, and software gave rise to digital SPECT technology, which in turn led to the D-SPECT. The D-SPECT, specifically designed for cardiac imaging, offers improvements in sensitivity and energy resolution over traditional Anger cameras (Goshen et al., 2018; Gambhir et al., 2009), faster scanning, dose reduction, more patient friendly design, and dynamic scanning. Many of the weaknesses of traditional SPECT are thus claimed to be resolved by the D-SPECT.

1.2 Problem

Variations in the visualisation process of myocardial perfusion can (significantly) influence the outcome and in turn have consequences for patient treatment. Before dynamic scanning, the total tracer uptake, into the myocardium, is evaluated by a nuclear physician. He/she must determine, based on a relative intensity image, if the patient has a degree of atherosclerosis or an other form of CVD. Quantitative measurements, for example those obtained by dynamically scanning with the D-SPECT, allow the nuclear physician to make more objective diagnoses.

The D-SPECT has been employed in Japan, Canada, France, and Great-Britain, but is rather new in the Netherlands. The relatively small Dutch patient population forces clinics to choose less expensive options, i.e. the D-SPECT. However, the D-SPECT's quantitative results must still be validated against well-known baselines such that the precision, accuracy, and reliability can be evaluated.

1.3 Goal

A validation study can be carried out by performing animal, human, or phantom experiments. Animal and human experimentation are disregarded based on ethical arguments alone. Therefore, to validate the D-SPECT dynamic scanning, a phantom validation study must be carried out. The primary goal of the master thesis is to develop a myocardial perfusion phantom, which can validate the D-SPECT's quantitative measurements, and answer the main research question:

Can patient treatment reliably depend on the D-SPECT, using dynamic scanning, in myocardial perfusion imaging?

- What are the primary requirements that the phantom must meet?
- What perfusion phantoms do already exist and are they suitable?
- How can the phantom meet the clinical requirements and mimic the perfusion of a human heart?

1.4 Primary requirements

The perfusion phantom must:

- be compatible with clinical software;
- have a system-based Arterial Input Function (AIF) with coupled myocardial Time-Activity Curve (TAC) which are equivalent to clinical practice [1];
- be of comparable physical size;
- model a 2^{nd} compartment;
- have the ability to simulate defects in an anatomical manner.

1.5 Boundaries

This master thesis is on the *development* of a myocardial perfusion phantom for which 28 weeks are available. The development of the phantom, combined with a validation study, will require more time than the available weeks.

[1] A system-based AIF will have a more natural response. By manually setting the AIF, simplifying assumption have to be made to prevent a high complexity, especially when a defect is simulated.

1.6 Approach

The project is carried out using the V-model (Rook, 1986) as proposed by Osborne et al. (2005) and will be divided into two main phases. The focus of the first phase is to develop a proof-of-concept phantom which will demonstrate direct compatibility with clinical software. The focus of the second phase, is, based on the insights gained from the first phase, to improve and/or modify the perfusion phantom. Ideally, the second phase yields a phantom that is, in the clinical software, indistinguishable from a human heart.

1.6.1 Phase 1

Phase 1 experiments are to prove that a semi-realistic phantom can be developed that meets the primary requirements. The phantom itself does not have to resemble an actual heart. However, the SPECT image of the phantom, must be, as seen from the quantification software, indistinguishable from a human heart. Dynamic flow experiments will be conducted to determine the software compatibility and to determine possible points of improvement.

1.6.2 Phase 2

Phase 2 experiments are used to determine if the phantom meets the primary requirements. The outcome of these experiments are used for the research questions, the discussion, the conclusion, and the recommendations.

1.7 General concept

The general concept, as shown in figure 1.1, shows a schematic outline of the involved systems.

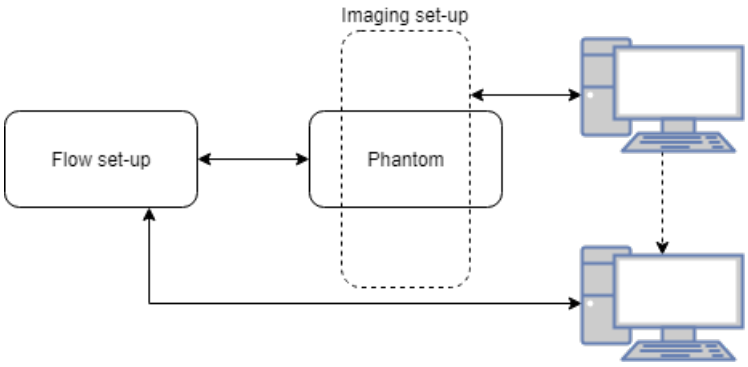

Figure 1.1: General concept, schematic overview. The flow set-up generates and measures the flow, and can be controlled and monitored from a connected computer. The phantom, part of the flow set-up but shown separately due to its importance, is placed in the Field Of View (FOV) of the imaging set-up. The imaging set-up has a dedicated workstation. Data can be retrieved from the workstation and transferred to the computer manually.

1.8 Document overview

Chapter 2 first gives background information on various subjects. It continues with a summary of prior work where the second sub-research question is answered. Chapter 3 provides a theoretical background to the flow, in a concept phantom, and determines the expected TAC. Chapter 4 shows detailed designs of the set-up, the phantom, the digital filter, and the Graphical User Interface (GUI). The results are shown in chapter 5, which are discussed, along with all research questions, in chapter 6, followed by a conclusion, which answers, definitively, the main research question, in chapter 7. The thesis ends with the recommendations in chapter 8.

This page is intentionally left blank.

2 Background

This chapter first introduces background information on traditional SPECT and its technology. It continues by providing background information on the D-SPECT, the tracer, Time-Activity Curves (TACs), and introduces a basic two-compartment model (more complex models are used to determine myocardial perfusion). The chapter ends by giving an overview of prior work, more specifically on previously developed perfusion phantoms (not limited to myocardial perfusion), and answers the second sub-research question.

2.1 SPECT

SPECT, or Single-Photon Emission Computed Tomography, is a nuclear imaging technique, using a gamma-emitting radioisotope, to generate tomographic images of a person (or object).

2.1.1 Traditional SPECT

Traditional SPECT scanners, see figure 2.1a, use Anger Cameras, see figure 2.1b, which use a configuration of collimators, see figure 2.1c, scintillators, and PMTs, see figure 2.1d, to generate an image based on received gamma radiation emitted by radioisotopes.

Collimator

The collimator, see figure 2.1c, essentially acts as a directional lens. It ensures that only a beam of particles, or waves, that are (almost) aligned with the collimator, pass. The gamma rays that pass the collimator, and are thus properly aligned, end up in the scintilator.

Scintillator

When a scintillator is excited by ionising radiation, for example by gamma rays, it exhibits scintillation. This form of luminescence, the emission of light not caused by incandescence, is a molecular propererty of certain molecules. Scintillators for gamma rays are, for example, comprised of Sodium Iodide, Caesium Iodide crystals or Cadmium Zinc Telluride (CZT). In case of an Anger camera, photons, emitted by the scintillator, are caught by a photocathode in the photomultiplier tube.

Photomultiplier tubes

A photomultiplier tube can be seen in the detailed view of an Anger camera, figure 2.1d. The photocathode is a negatively charged electrode, coated with a photosensitive compound, which emits an electron when hit by a photon. The emitted electron passes through a focussing electrode, which guides the electron towards the first dynode, a positively charged electrode. When the electron hits a dynode, it triggers secondary emission, emitting more electrons than it absorbs. The emitted electrodes in turn hit another dynode, each triggering secondary emission, whose electrons hit, yet again, another dynode. This effect cascades down to the last electrode, called the anode. The anode, which is held close to ground potential, is connected to connector pins. The electrons hitting the anode cause a current pulse, which is easily detected on the connector pins.

(a) A Discovery NM630 SPECT scanner, retrieved from GE healthcare. The patient bed, left, moves between the detectors, middle. The detectors' gantry can rotate to capture gamma radiation in different directions.

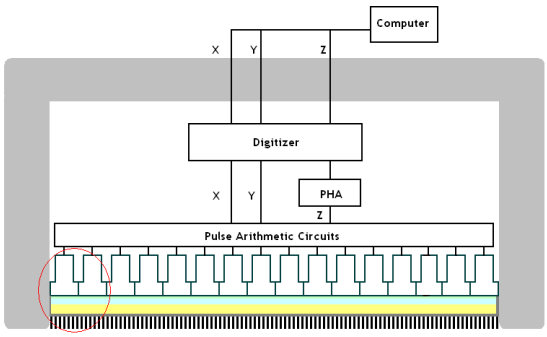

(b) Schematic of an Anger camera, retrieved from Wikipedia. Detailed view in figure 2.1d. Each column provides a sharp current pulse caused by the scintillation and the photomultiplier process which is caught by Pulse Arithmetic Circuits. These circuits provide dimensional information of the origin of captured X-Rays. The Pulse-Height Analyser (PHA) accepts pulses of varying heights and creates histogram. All information is digitised and sent to a computer for processing.

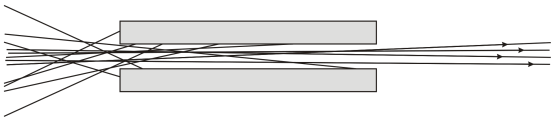

(c) Schematic of a collimator, retrieved from Wikipedia. Beams that are not aligned with the collimator do not pass through and are thus not captured by a scintillator lying behind the collimator in an Anger camera.

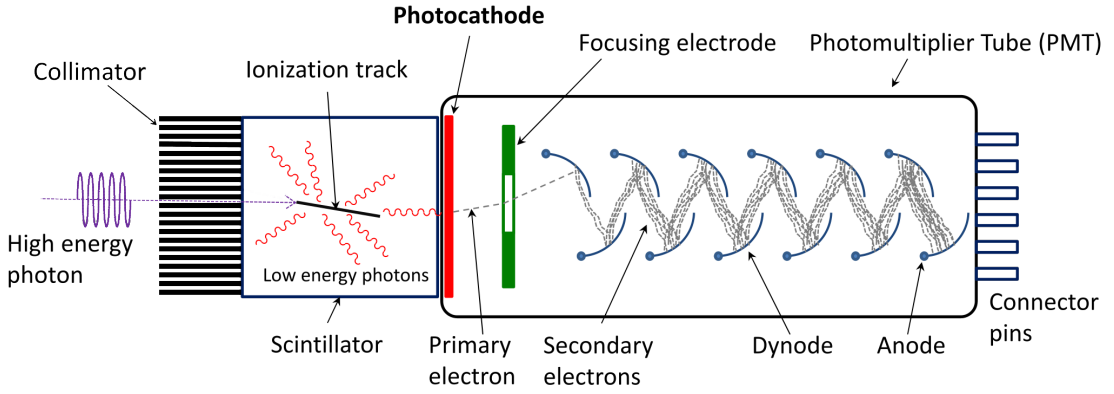

(d) Detailed view of figure 2.1b, adapted from Wikipedia. High energy photons, also known as gamma Rays, pass through the collimator, when aligned, and enter the scintillator. The scintillator reacts to a gamma ray and generates visible light. A photocathode, in the PMT, reacts to the visible light and emits a primary electron. A focusing electrode directs the electron to the first dynode. It then "bounces" on multiple dynodes; each bounce causing secondary emission, creating more electrons that can bounce on subsequent dynodes. The electrons hit the anode, causes a sharp current pulse on the connector pins, which can be detected by electronics.

Figure 2.1: An example of a SPECT scanner and a schematic explanation of an Anger camera.

2.1.2 Solid-State technology

Numerous developments in imaging systems, detectors, and software resulted in Solid-State detectors based on CZT. Wagenaar (2004) developed pixelated CZT detector units, which allows it to be used for medical imaging applications. A CZT detector can operate in direct-conversion mode at room temperature whilst other Solid-State detector materials, for example Germanium, requires liquid nitrogen cooling to ensure proper Signal-to-Noise Ratio. The direct-conversion of photons, by Solid-State detectors, render PMTs unnecessary, and CZT's direct conversion mode at room temperature, allows for more compact and flexible designs (Erlandsson et al., 2009). However, CZT is difficult to work with, resulting that, worldwide, only four companies manufacture CZT.

2.1.3 D-SPECT

The D-SPECT, see figure 2.2, developed by Spectrum Dynamics, uses 9 pixelated (16x64) CZT detector units with Tungsten collimators. These Tungsten collimators have larger square holes than standard lead parallel-hole collimators. It allows for 8 times more acceptance of gamma rays which, however, also include more scatter. In addition, the detectors can rotate and translate which enables imaging from hundreds of different angles (Erlandsson et al., 2009). The D-SPECT is specifically designed for cardiac imaging. Its design, see figure 2.2 and 2.3, is more patient friendly than traditional gantry-based scanners. It is able to perform dynamic myocardial perfusion imaging allowing for quantitative measurements. Its temporal resolution is variable. To capture the AIF, frames are taken every 3 seconds for the first 60 seconds, i.e. the first 20 frames. During the remainder of the scan, frames are taken every 30 seconds.

2.2 Tracer

The standard tracer used for SPECT imaging, Technetium ^{99m}Tc Tetrofosmin, is specifically used to assess myocardial perfusion. It is developed by GE Healthcare and was approved on 9th February, 1996 by the FDA (The United Stated Food and Drug Administration). The tracer has a good myocardial uptake and retention. Imaging can be performed 15 minutes post injection for stress perfusion and 30-60 minutes post injection for rest perfusion. Ischemia can be identified through evaluation of the tracer's uptake, by looking at the intensities in the images. Areas with less uptake, have a lower colour intensity than areas with high uptake. However, the brightest colour does not guarantee "high" uptake, rather it is the area with the *most* uptake compared to all other areas. A nuclear physician will have to evaluate if there is sufficient perfusion.

Dynamic scanning solves this problem by quantifying the blood flow. The gamma rays, due to the decay of the tracer, is captured by the scanner, resulting in TACs. Mathematical models are then able to determine the blood flow. The quantitative outcome will give the nuclear physician the ability to make an objective decision regarding patient treatment.

2.3 Time-Activity Curves

A TAC, shown in figure 2.4, shows the activity of a certain ROI over time. For the D-SPECT, the first 20 frames are taken every 3 second, while the remainder is taken every 30 seconds. The high frames per second (FPS) is required to extract the AIF and to determine first pass perfusion. After the first pass, the tracer is already absorbed by the myocardium and eliminates the benefits of a high FPS.

It can clearly be seen from figure 2.4, that the left ventricle chamber activity (green line, largest peak) returns to zero. The myocardial activity (other coloured lines) start with a peak activity (first pass) and maintain a small offset (myocardial uptake). A TAC graph is characterises by one large peak activity, called the AIF, and smaller peaks that maintain a small offset, called the myocardial activity.

Figure 2.2: The D-SPECT, retrieved from Spectrum Dynamics. The D-SPECT is specifically designed for cardiac imaging and its characteristic can clearly be seen: no gantry.

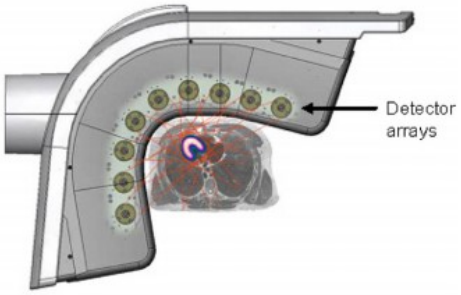

Figure 2.3: D-SPECT scanner head design (Erlandsson et al., 2009). Due to its unique design, and specialistic purpose, the D-SPECT's scanner head focusses on the heart, passively, and can focus actively by using rotating detector arrays to ensure compatibility with a variety of patients.

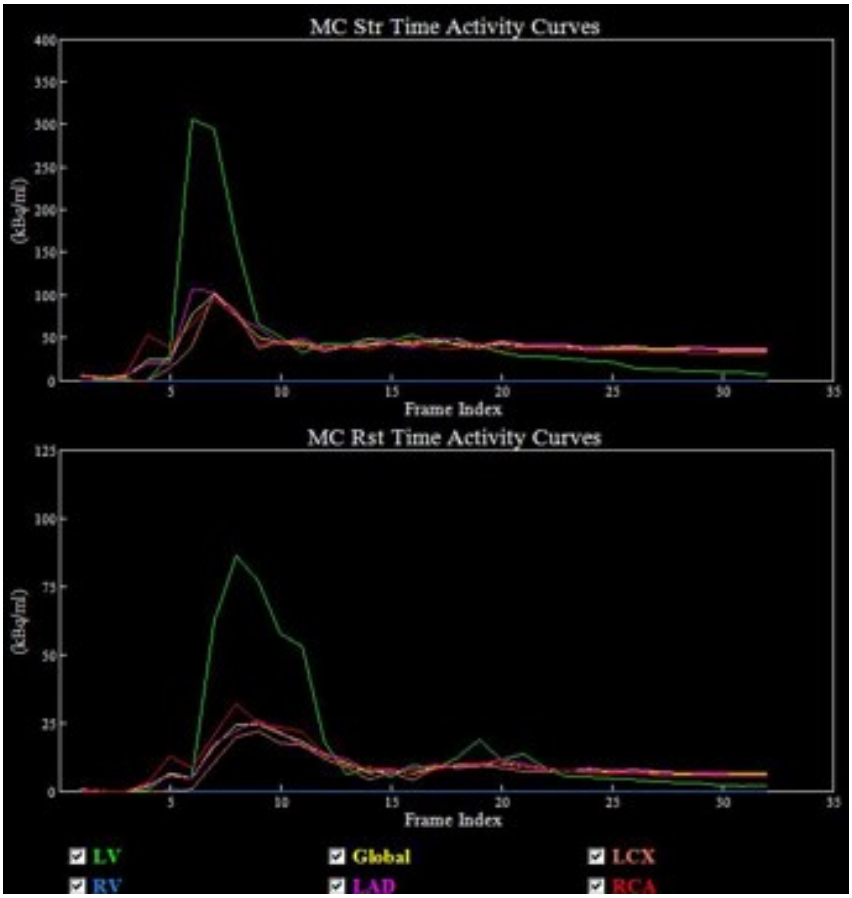

Figure 2.4: Typical TAC, with normal perfusion. Retrieved from Spectrum Dynamics. The curve with the largest peak is the activity in the left ventricle (LV) and is known as the AIF. The curves with the lower peaks correspond to the activity in the right ventricle, in segments of the myocardium corresponding to each coronary, and the combined average activity (global) in the myocardium. The Y-axis shows the average decays per second per mL in the ROI, the X-axis show the frames of the D-SPECT (first 20 taken every 3 seconds, others every 30 second).

2.4 Two-compartment model

A one-compartment model, where the tracer never leaves the supplying artery, will show the characteristic peaks, but will not maintain a steady offset in the myocardium. A multi-compartment model takes the outflow of tracer into tissue into account. A two-compartment model only takes one additional compartment into account, i.e. the myocardium, while higher compartment models also take additional compartments into account, e.g. inter-cellular space. The amount of tracer that is absorbed, held, and/or removed from the myocardium depends on various factors and processes, e.g. removal by white blood cells, natural decay, concentration gradient, blood pressure, and permeability. (Carson, 2005) describes this relation as shown in equations 2.1 and 2.2. The precise interpretation is out of the scope of the project but it is important to note that the flux is dependent on permeability, capillary surface area, tracer concentrations, and the blood flow.

To simplify, the two-compartment model used in this thesis, assumes the supplying artery as the first compartment and the myocardium the second. A phantom that allows tracer to exit the supplying artery into the tissue, see figure 2.5, will show the characteristic peaks (first pass), and maintain a steady offset in the myocardium, thus making the phantom study more comparable to patient studies. The natural decay of the tracer is neglected due to the relatively long half-life compared to the time it takes to perform a perfusion scan (typically a few minutes).

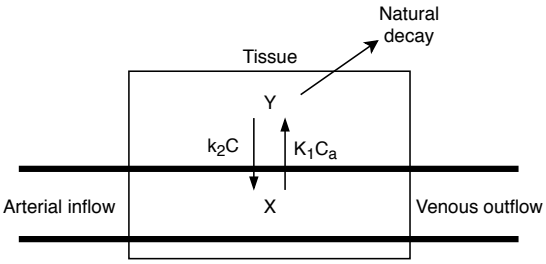

Figure 2.5: Simplified 2-compartment model, adapted from Carson (2005). The exchange of tracer is directly dependent on the concentration in both the artery and tissue. Due to pressure and concentration differences, tracer can exit the blood vessel and enter the tissue. Additionally, the tracer can decay naturally or exit the tissue back into the blood vessel.

$$J = J_{in}(t) - J_{out}(t) \tag{2.1}$$

$$\frac{dC}{dt} = K_1 C_a(t) - k_2 C(t) \rightarrow C(t) = C_a K_1 e^{-k_2 t} \tag{2.2}$$

where:

J = Net flux of tracer,
J_{in} = Influx of tracer,
J_{out} = Outflux of tracer,
K_1 = Rate of entry from blood to tissue = $F \cdot E \left[\frac{mL}{min}\, gram\right]$,
k_2 = Rate of return from tissue to blood $\left[\frac{1}{min}\right]$,
C = Tracer concentration in tissue, $\left[\frac{kBq}{gram}\right]$,
C_a, C_v = Tracer concentration in artery and vein $\left[\frac{kBq}{mL}\right]$,
E = Unidirectional extraction fraction: $E = 1 - e^{\frac{PS}{F}}$,
F = Blood flow $\left[\frac{mL}{min}/gram\right]$,
P = Permeability of the tracer across capillary surface $\left[\frac{cm}{min}\right]$,
S = Capillary surface area per gram of tissue $\left[\frac{cm^2}{gram}\right]$.

2.5 Prior work

Currently, as of Wednesday 10th July, 2019, no myocardial perfusion phantoms have been developed specifically for D-SPECT. However, phantoms have been developed for CT, MR, and ultrasound which can potentially be used to validate the D-SPECT.

2.5.1 Magnetic resonance

Noguchi et al. (2007) developed a phantom that is made of a syringe filled with smaller tubes. Perfusate enters the syringe and flows through beads, to disturb the flow and to ensure a better distribution.

Ebrahimi et al. (2010) developed a phantom by using micro-fabrication to create microvasculature on silicone wafers. The perfusate originates from a single input, the "artery", and travels via many different paths to the singular output, the "vein".

Wang et al. (2010) used a haemodialysis filter to mimic human tissue flow at a wide range of flow rates. Anderson et al. (2011) extracted fibres from such haemodialysis filter to create their own single-fibre, and multi-fibre, phantom. Similar to some standard haemodialysis filters, their phantom has access to the extracellular space, i.e. a 2^{nd} compartment.

Chiribiri et al. (2013) developed a four chambered phantom that resembles the heart of a 60kg person. The four chambers correspond to the chambers of the heart, and are matched to physiological size. In addition, the vena cava, the pulmonary artery/vein combination, and an aorta are present in the phantom. Contrast travels from the right atrium to the left ventricle, via the pulmonary artery/vein combination and left atrium. After the left ventricle, the contrast travels through the aorta where a part of the flow flows to a separate myocardium. The same phantom is used by Otton et al. (2013) to compare CT against MRI.

O'Doherty et al. (2017) used a water-filled torso phantom with static cardiac inserts. The addition of the torso phantom ensures that images are more closely related to those taken of a person; the torso phantom has lungs, a liver, and a vertebrae.

2.5.2 Computed Tomography

Teslow and Robb (1991) have developed a cylindrical perfusion phantom based on the left ventricle of a dog. The inside of the ventricle is a solid plastic cylinder with an equivalent X-Ray attenuation to that of a blood filled ventricle. The myocardium surrounds the solid cylinder, as one large chamber, and is filled with different sized beads. It is supplied with perfusate by a single inlet and and is drained by two outlets.

Klotz and König (1999) used a lucite cylinder filled with small grannulae that have been heated and compressed, for increased packing density. It is placed in a 20cm water phantom for comparable attenuation.

Driscoll et al. (2011) developed a 2-compartment cylindrical phantom where the capillaries are simulated by means of a vinyl tube with small holes for mass exchange. The output of the vinyl tube and cylinder, separately pass through regulator valves before being combined. The ratio between the two outputs can be altered by varying the regulator valves. Their AIF is created by means of a programmable pump which injects tracer in the form of a typical, clinical AIF.

Ganguly et al. (2012) developed a linearly moving, cylindrical phantom. The goal is to compare and determine the temporal accuracy of the imaging system. Their phantom was placed in a cylindrical, water-filled, phantom for proper attenuation.

Mathys et al. (2012) developed a similar phantom that consists of a cylinder inside a larger cylinder. Water flows via four tubes into the inner cylinder, where it then flows outward into the larger cylinder. The larger cylinder contains polyoxymethylene globes as tissue mimicking material.

Boese et al. (2013) developed a cylindrical phantom that utilises a combination of large arteries that splits into smaller arteries, and in turn split into even smaller arteries. Ultimately, the smallest arteries connect to a sinter board (mimics capillary network by having many pores), with porosity volume of 35%.

Suzuki et al. (2017) uses a dry-type haemodialyser with a pressurised dialysate space to prevent perfusate from leaving the hollow fibres, effectively eliminating the 2^{nd} compartment. The haemodialyser is placed in an X-Ray absorbing, polyurethane resin filled body to simulate normal brain tissue. Hashimoto et al. (2018) used the same phantom but with a commercially synthetic bone layer such that quantification software recognises a human head.

2.5.3 Ultrasound

Veltmann et al. (2002) have designed a flow set-up that consists of a high- and low flow rate circuit. Perfusate from a heated reservoir is pumped, at high flow rates, through a haemodialysis cartridge, to filter residue micro-bubbles (contrast agent in ultrasound) and removes air bubbles. The perfusate then enters a second haemodialysis cartridge, called the perfusion cartridge. New micro-bubbles are injected just before this perfusion cartridge. A gear pump, at low pump speed, after the perfusion cartridge controls the amount of perfusate through the cartridge, which then passes through a third haemodialysis cartridge to filter the micro-bubbles. Perfusate that does not pass through the perfusion cartridge passes directly back to the heated reservoir. This phantom is used by both Sakano et al. (2015) and Lohmaier et al. (2004).

Kim et al. (2016) performed perfusion experiments using haemodialysis cartridge without any contrast agent. However, they did use a second, peristaltic pump to simulate cardiac motion.

2.5.4 Discussion

The most important requirements for the phantom are: compatibility with clinical software, a system-based AIF, and a coupled myocardium. The compatibility with clinical software is directly linked to the validation: it cannot be validated if modifications are required to ensure compatibility with the phantom. A system-based AIF will be more natural and consistent, especially when defects are simulated. Any variation can have (unforeseen) consequences if the AIF is manually generated. A coupled myocardium will be more natural and consistent with the AIF, as it is in a human body.

Most phantoms are (significantly) simplified models. However, some phantoms show interesting characteristics, specifically phantoms by Teslow and Robb (1991), Driscoll et al. (2011), Mathys et al. (2012), and Chiribiri et al. (2013).

The phantom by Teslow and Robb (1991) is designed to resemble the left ventricle of a dog's heart. The cross-sectional images are equivalent to that of a human, see figure 2.6. Their results show a poorly perfused cross-sectional slice (especially the top section), see figure 2.7. The most likely cause is the singular inlet at the bottom of the phantom. The primary flow path will be from the inlet to the bottom outlet rather than to the top outlet.

The phantom by Driscoll et al. (2011) resembles the phantom of Teslow and Robb (1991). Instead of using a beads-filled myocardium, Anderson et al. (2011) uses a tube that revolves on the inside of the cylinder, with holes to approach a 2-compartment model. However, the 2^{nd} compartment is a free flowing compartment rather than a "trapping" compartment. Furthermore, their AIF is specifically generated by a programmable pump rather than being system-based. It is able to manually tune the ratio between the flow that exits the primary flow path by using two valves, one for the main flow path and one for the free flowing compartment.

The phantom by Mathys et al. (2012), shows again a cylindrical phantom. Instead of a single, 360°, myocardium, their phantom has four, 90°, segments, filled with polyoxymethylene beads, around a central cylinder. The inlet is located in the central cylinder with holes to the outer

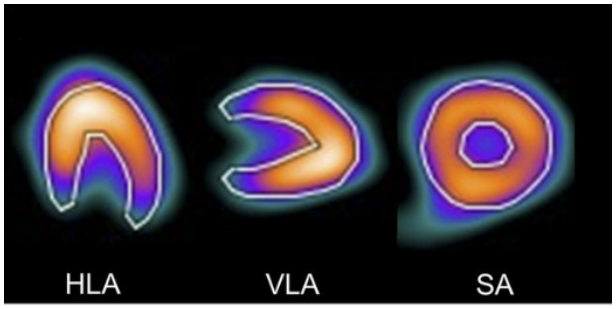

Figure 2.6: Normal cross-sectional images of the left ventricle retrieved using a D-SPECT (Yoneyama et al., 2017).

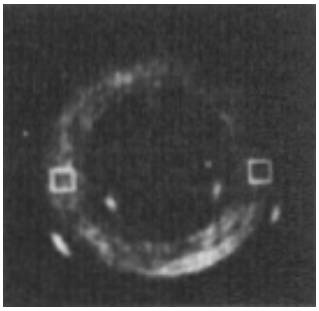

Figure 2.7: The Short Axis (SA) cross-sectional image of the phantom by Teslow and Robb (1991).

segments. The phantom is able to have a system-based AIF along with a myocardial TAC, but is unable to trap the contrast.

The phantom by Chiribiri et al. (2013), is, with its four heart chambers, most equivalent to a human heart. However, the myocardium is a separate cylinder, which does not cover the left ventricle.

What perfusion phantoms do already exist and are they suitable?

Several phantoms show interesting characteristics. Although most phantoms meet the last two requirements, they are typically not directly compatible with clinical software. Clinical software is biased towards the shape of the heart, see figure 1 and 2.6. The phantom developed by Teslow and Robb (1991) has the correct SA slice, but lacks an apex or an AIF. Driscoll et al. (2011) added the AIF, which is manually programmed, but still lacks an apex. Therefore, to meet the clinical and the primary requirements, a new myocardial perfusion phantom must be developed.

3 Analysis

This chapter describes the theoretical background for the concept myocardial perfusion phantom. The concept phantom has a centralised cylinder, mimicking the left ventricle, and a surrounding myocardium. The myocardium is split into three equal chambers according to clinical models. The left ventricle output, or interchangeably called the aorta, branches to each myocardial chamber, similar to the coronary arteries. The primary flow is generated by a pump whereas the secondary flow, i.e. myocardial flow, is indirectly regulated by means of flow regulators. The chamber itself contains three tubes, with holes, to simulate a two-compartment model. Tracer can exit through these tubes and circulate in the chamber. The flow in the chamber is expected to be (significantly) lower than in the tubes, mimicking the "trapping" behaviour.

The AIF and TACs of the phantom, see figure 3.1 can be estimated by using the volume continuity principle, as given in equation 3.1. The continuity of volume assumes steady flow and ignores frictional losses. Flow is typically steady when the Reynolds number, see equation 3.2, is less than 2300, and can be verified at the end, when the velocities have been determined.

$$Q = Av = CONSTANT \tag{3.1}$$

$$Re = \frac{\rho v D}{\mu} \tag{3.2}$$

Where:

A = Cross-sectional area $\left[m^3\right]$,
ρ = Density of fluid $\left[\frac{kg}{m^3}\right]$, water is 997 $\left[\frac{kg}{m^3}\right]$,
v = Velocity of fluid $\left[\frac{m}{s}\right]$,
Re = Reynolds number,
μ = Dynamic viscosity $[Pa \cdot s]$, water at 20°C is 1.0016 $[mPa \cdot s]$.

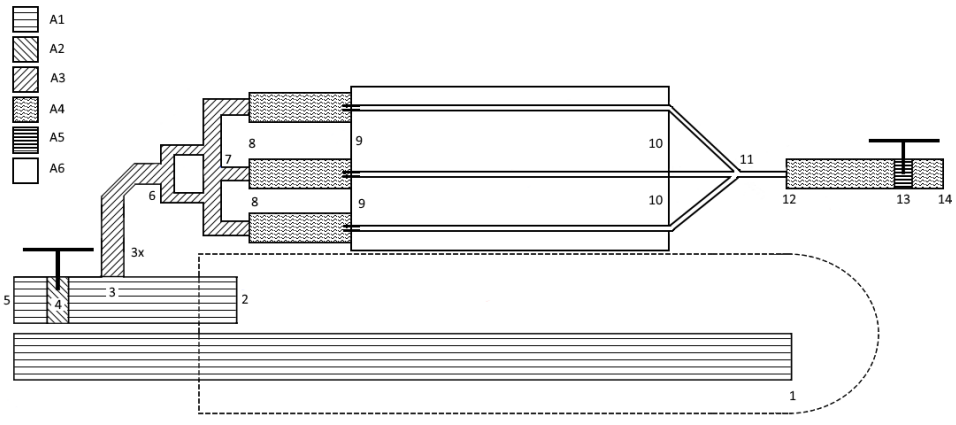

Figure 3.1: Schematic overview of phantom. The flow enters the phantom from the bottom left and exits the phantom at point 5. A flow regulator is placed at points 4 and 13. The regulator can increase or decrease the flow-area, altering the pressure drop across the regulator. The ratio between the pressure drop at points 4 and 13 regulates the flow rate to the myocardium (tube 3 to 6). Only one of the three myocardial chambers is shown.

The areas A2 and A5 are variable. The flow regulators can be tightened, decreasing the cross-sectional area and thus increasing the pressure drop across the regulator. The flow regulators can be loosened, increasing the cross-sectional area and thus decreasing the pressure drop across the regulator. The ratio between the areas of the outlet flow regulator (point 4, figure 3.1) and the myocardium flow regulators (point 13, figure 3.1), defines the flow passing through the myocardium. The remainder of the areas are based on the aortic tube, myocardial tubes, and printed tracks (based on the dimensions of Luer connectors). The system parameters, as used in the theoretical model, are:

$$
\begin{aligned}
Q_{in} &= \text{Assumed } 2.5\left[\tfrac{L}{min}\right] = 4.167\cdot 10^{-5}\left[\tfrac{m^3}{s}\right],\\
Q_{myo} &= \text{Assumed } 100\left[fracLmin\right] = 1.667\cdot 10^{-6}\left[\tfrac{m^3}{s}\right],\\
A_1 &= 5.026\cdot 10^{-5}\left[m^2\right],\\
A_3 = A_6 &= 4.47\cdot 10^{-5}\left[m^2\right],\\
A_4 &= 2.827\cdot 10^{-5}\left[m^2\right],\\
D_{A_1} &= 8\,[mm],\\
D_{A_6} &= 0.0094" = 2.3876\,[mm],\\
D_{1\,A_2} &= 38\,[mm].
\end{aligned}
$$

A parameter of the fluid flow, Z, in a certain part of the phantom, from a point X to a point Y, is written as: ${}^{X}Z_{Y}$.

The main aortic flow, flows through tube 1 into the left ventricle where it can only exit the phantom at point 2. The cross-sectional diameter of the left ventricle is 38 [mm]. Therefore:

$$
\begin{aligned}
{}^{in}Q_1 = 4.167\cdot 10^{-5} = A_1 \cdot {}^{in}v_1 = \pi(5.026\cdot 10^{-5})\cdot {}^{in}v_2 \qquad (3.3)\\
\rightarrow {}^{in}v_2 = \frac{4.167\cdot 10^{-5}}{5.026\cdot 10^{-5}} \approx 0.83\left[\frac{m}{s}\right]\\
{}^{1}Q_2 = 4.167\cdot 10^{-5} = {}^{1}A_2 \cdot {}^{1}v_2 = \pi(19\cdot 10^{-3})^2\cdot {}^{1}v_2 \qquad (3.4)\\
\rightarrow {}^{1}v_2 = \frac{4.167\cdot 10^{-5}}{\pi(19\cdot 10^{-3})^2} \approx 0.0367\left[\frac{m}{s}\right]
\end{aligned}
$$

The length of the ventricle is approximately 100 [mm], and the time for liquid to pass through the ventricle is thus:

$$
t = \frac{{}^{in}L_1}{{}^{in}v_1} + \frac{{}^{1}L_2}{{}^{1}v_2} = \frac{100\cdot 10^{-}3}{0.83} + \frac{100\cdot 10^{-}3}{0.0367} = 2.72 + 0.12 = 2.84[s] \qquad (3.5)
$$

A typical injection, in clinical practice, is an injection of $500\cdot 10^{6}Bq$. Assuming the tracer is a 0 dimensional entity, i.e. a point, it will stay approximately 2.84 seconds in the left ventricle.

Volume continuity can be used to determine the velocity in the myocardial chamber. Part of the total volume to the myocardial will exit the primary tubes and enter the chamber itself. To simplify, it is assumed that the volume distributes itself equally over the three tubes and the myocardial chamber:

$$
\begin{aligned}
Q_{myo} = 1.667\cdot 10^{-6} = 4\cdot {}^{9}A_{10}\cdot {}^{9}v_{10} = (4.47\cdot 10^{-5})\cdot {}^{9}v_{10} \qquad (3.6)\\
\rightarrow {}^{9}v_{10} = \frac{1.667\cdot 10^{-6}}{4\cdot(4.47\cdot 10^{-5})} = 9.32\cdot 10^{-3}\left[\frac{m}{s}\right]
\end{aligned}
$$

The time tracer is in one of the three tubes of the myocardium, is:

$$t = \frac{L_{myo}}{{}^{9}v_{10}} = \frac{74.5 \cdot 10^{-3}}{9.32 \cdot 10^{-3}} = 7.99[s] \tag{3.7}$$

However, only a part of the injected activity, i.e. $500 \cdot 10^6 Bq$, passes through the myocardium. The ratio between myocardial flow and aortic flow, is $\frac{Q_{myo}}{Q_{in}} = \frac{100[\frac{mL}{min}]}{2500[\frac{mL}{min}]} = {}^{1}/_{25}$. Therefore, only ${}^{1}/_{25} \cdot {}^{1}/_{4} \cdot (500 \cdot 10^6) = 5 \cdot 10^6 Bq$ passes through each tube.

The tracer can exit the main flow tubes, where the area is larger and thus the velocity is lower. Each chamber is ${}^{1}/_{3}$ of a full circle (see figure 3.2), with an inner radius of 23 [mm] and an outer radius of 34 [mm]. The tubes itself have a diameter of 6.4 [mm] and thus a cross-sectional area of $\pi \cdot (3.2 \cdot 10^{-}3)^2 = 3.217 \cdot 10^{-5} \left[m^2\right]$. The cross-sectional area of the chamber is then:

$$A_{chamber} = \frac{1}{3}\pi \cdot \left((34 \cdot 10^{-3})^2 - (23 \cdot 10^{-3})^2\right) - 3 \cdot 3.217 \cdot 10^{-5} = 5.601 \cdot 10^{-4} \left[m^2\right] \tag{3.8}$$

The velocity in the chamber itself, assuming equal distribution of the volume:

$$\begin{aligned} Q_{myo} = 1.667 \cdot 10^{-6} = 4 \cdot A_{chamber} \cdot v_{chamber} = (5.601 \cdot 10^{-4}) \cdot v_{chamber} \\ \rightarrow v_{chamber} = \frac{1.667 \cdot 10^{-6}}{4 \cdot (5.601 \cdot 10^{-4})} = 7.44 \cdot 10^{-4} \left[\frac{m}{s}\right] \end{aligned} \tag{3.9}$$

The time tracer is in the chamber itself:

$$t = \frac{L_{myo}}{v_{chamber}} = \frac{74.5 \cdot 10^{-3}}{7.44 \cdot 10^{-4}} = 100.13[s] \tag{3.10}$$

Knowing the velocities in each area of interest, the Reynolds numbers can be determined:

$${}^{in}Re_1 = \frac{\rho \cdot {}^{in}v_1 \cdot {}^{in}D_1}{\mu} = \frac{997 \cdot (0.83) \cdot (8 \cdot 10^{-3})}{1.0016 \cdot 10^{-3}} = 6609 \tag{3.11}$$

$${}^{1}Re_2 = \frac{\rho \cdot {}^{1}v_2 \cdot {}^{1}D_2}{\mu} = \frac{997 \cdot (0.0367) \cdot (38 \cdot 10^{-3})}{1.0016 \cdot 10^{-3}} = 1388 \tag{3.12}$$

$${}^{9}Re_{10} = \frac{\rho \cdot {}^{9}v_{10} \cdot {}^{9}D_{10}}{\mu} = \frac{997 \cdot (9.32 \cdot 10^{-3}) \cdot \left(2.3876 \cdot 10^{-3}\right)}{1.0016 \cdot 10^{-3}} = 22 \tag{3.13}$$

The Reynold's number for the input tube, equation 3.11, shows that the flow is turbulent (i.e. Reynold's number » 2300). Therefore, the trajectory of the tracer is non-laminar and thus the tracer will be in this area for a longer period of time, widening the AIF. From equations 3.12 and 3.13 it can be seen that the flow is expected to be non-turbulent. Therefore, the time estimate is more closely related to reality. The Reynolds number for the chamber itself cannot be calculated without the hydraulic diameter, D_H, see figure 3.2 and equation 3.15. The reynolds number for the chamber is:

$$Re_{chamber} = \frac{\rho \cdot v_{chamber} \cdot D_H}{\mu} = \frac{997 \cdot (7.44 \cdot 10^{-4}) \cdot (26.8 \cdot 10^{-3})}{1.0016 \cdot 10^{-3}} = 19 \tag{3.14}$$

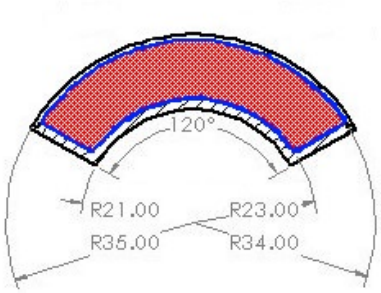

Figure 3.2: Hydraulic diameter of a myocardial chamber. The blue perimeter is the wetted perimeter, P. The red area is the cross-sectional area of the flow., A

$$D_H = \frac{4A}{P} = 0.0268\,[m] \tag{3.15}$$

$A = A_{chamber}$ (equation 3.8) $= 5.601 \cdot 10^{-4}\,[m^2]$
$P = \frac{2\pi}{3} \cdot (R_{out} + R_{in}) + 2 \cdot (D_{out} - D_{in} \approx 83.69 \cdot 10^{-3}\,[m]$

Expected TACs

The expected Time-Activity Curve is shown in figure 3.3. The AIF, due to the Reynolds number, is expected to be wider than shown. Additionally, the expected TAC is based on several assumptions:

- The tracer is a 0 dimensional entity;
- No turbulent flow in the areas of interest;
  Left ventricle and myocardial chamber.
- No frictional losses;
- The pump has an infinite capacity;
  In reality, the pump cannot provide infinite pressure to realise any volumetric flow rate.
- Tracer distribution in the phantom is equivalent to the flow distribution;
  The amount of tracer activity to the myocardium according to the ratio of the myocardial flow rate to the input flow rate.
- All radiation, caused by the decay of the tracer, is captured by the scanner.

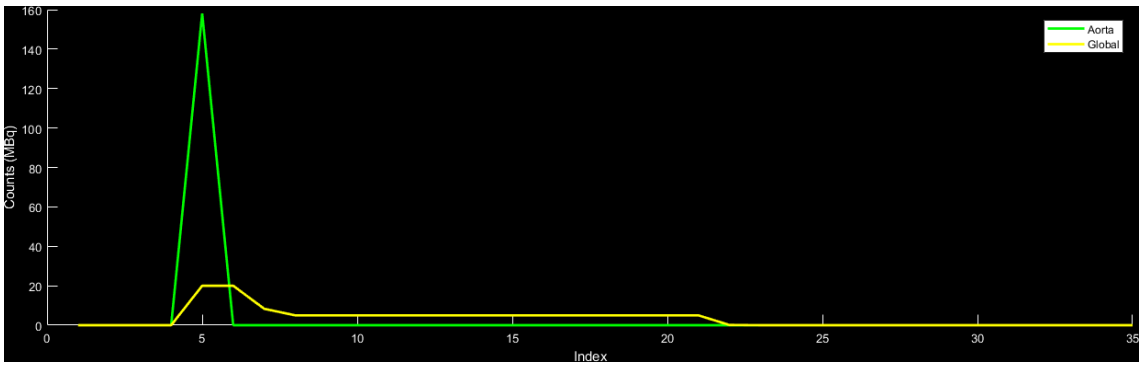

Figure 3.3: Theoretical Time-Activity curve of perfusion phantom based on several simplifying assumptions.

4 Design

This chapter describes the myocardial perfusion phantom's design in more detail. First, the configuration of the overall set-up and the design of the phantom (each phase separately) are discussed. The chapter ends by describing the digital filter and Graphical User Interface (GUI) designs.

4.1 Phantom

The radiation exposure, due to the D-SPECT's tracer Technetium ^{99m}Tc Tetrofosmin, is limited for patients that undergo myocardial perfusion imaging. After injection, the tracer decays naturally and the patient excretes part of the tracer. However, lab technicians are exposed for a longer period of time. The radiation burden stays within acceptable limits when the tracer is injected into a patient. The phantom, however, blocks less radiation than a human body, making the radiation burden larger for everyone in the room with the phantom. Through proper protocol and short exposure time (typically 3 hours on an experimentation day), the radiation burden is limited. Should the tracer leak from the phantom, it must be properly cleaned to prevent contamination of the room, which costs time and money. Therefore, a leak is highly undesirable.

Waste water, which is contaminated with the tracer, will keep radiating the environment. In an open-circuit configuration, see figure 4.1, contaminated waste water must be collected in closable containers and be placed in a sealed, lead-lined room until the tracer has naturally decayed to safe limits. However, it may be possible to filter the tracer from the water in a closed-circuit configuration, see figure 4.2. The tracer will then be located in the filter and/or in a separate waste container. Both must be placed in a sealed, lead-lined room until the tracer has naturally decayed to safe limits. However, as of Wednesday 10$^{\text{th}}$ July, 2019, it has not been proven that the tracer can be filtered from the waste water. The phantom will thus use an open-circuit configuration.

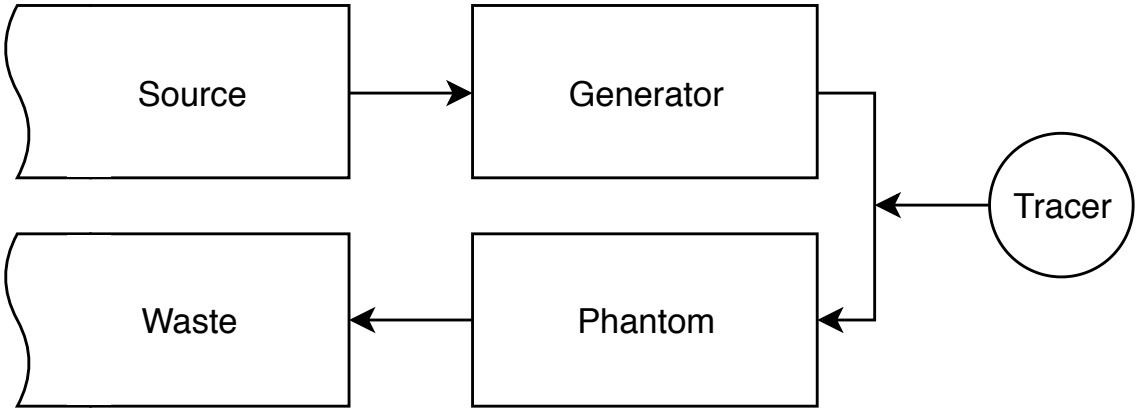

Figure 4.1: Open-Circuit configuration. Water is pumped through the phantom by a flow generator (e.g. pump). The water is deposited in a waste container. The source and waste container are not connected. Only the (large) waste container will maintain a radiation source.

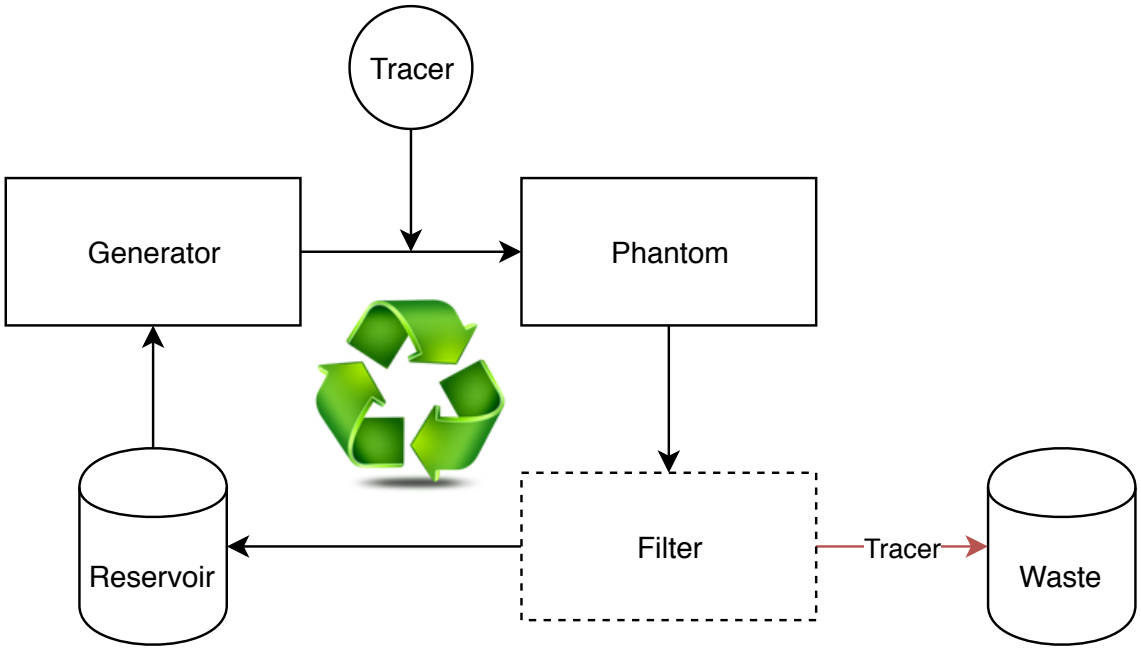

Figure 4.2: Closed-Circuit configuration. Water is pumped through the phantom by a flow generator (e.g. pump). The water passes through a filter where the tracer is extracted from the water and stored in a separate container. The cleaned water returns to the source container. Only the (small) waste container will maintain a radiation source.

4.1.1 Phase 1

The phase 1 phantom design can be seen in figure 4.3. It resembles a simplified left ventricle (the central, hollow, cylinder), which can clearly be seen in figure 4.3c. The phantom contains a unique characteristic: a surrounding, three-segment, modular myocardium. Each segment represents a segment from the 4DM vascular model, 4.3b. The physical segments are placed under a different angle such that they are more easily and, more importantly, better reproducibly placed onto the ventricle.

The main pump is connected to the bottom connection in figure 4.3c. A tube is inserted into the left ventricle to ensure the water reaches the tip of the central cylinder with limited recirculation. The outlet has a built in side-branch to ensure a physiological and better related myocardial TAC, coupled to the AIF. The myocardial chambers surround the ventricle chamber, as it does in an actual human heart. The first phase design is for a proof-of-concept phantom, and therefore lacks an apex such that the phantom is more easily designed and realised.

Figure 4.3d shows an overview of the different systems. The control module measures the flow and controls the pump to maintain a constant flow. The flow-feedback circuit consists of a Doppler flow sensor and a submersible pump. The myocardial flow sensors, placed after the phantom, are smaller turbine sensors with a special insert to measure flows as low as 30 mL/min. All measurements are first fed into separate digital filters to remove high frequency noise components and are then send to a connected computer. The flow to the myocardium must be manually adjusted by setting the ratio between the flow regulators. The flow can be monitored, at 10Hz, in the GUI while making the adjustments to the myocardial flow.

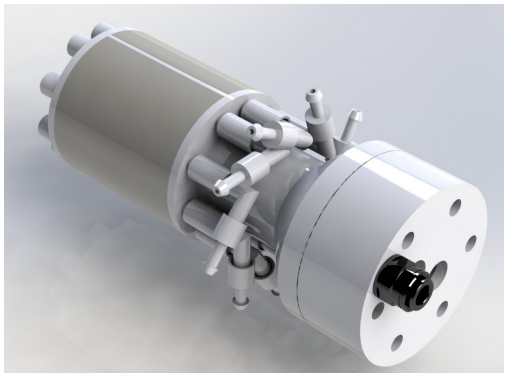

(a) Outer design. The black John Guest connector on the right side will branch eight times. Each branch is connected to the Luer connectors in the middle. De myocardial chambers, left, have detachable lids.

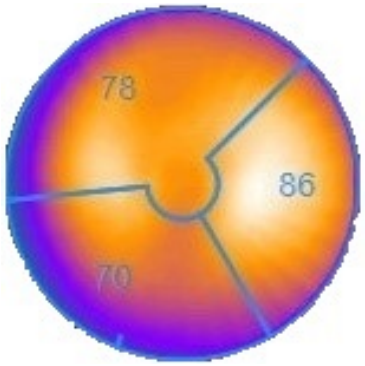

(b) Vascular model (NG1). This model is used by 4DM. Each area is supplied by one of the coronary arteries. The values are the determined perfusion values in mL/min/gram, i.e. the perfusion values that require validation.

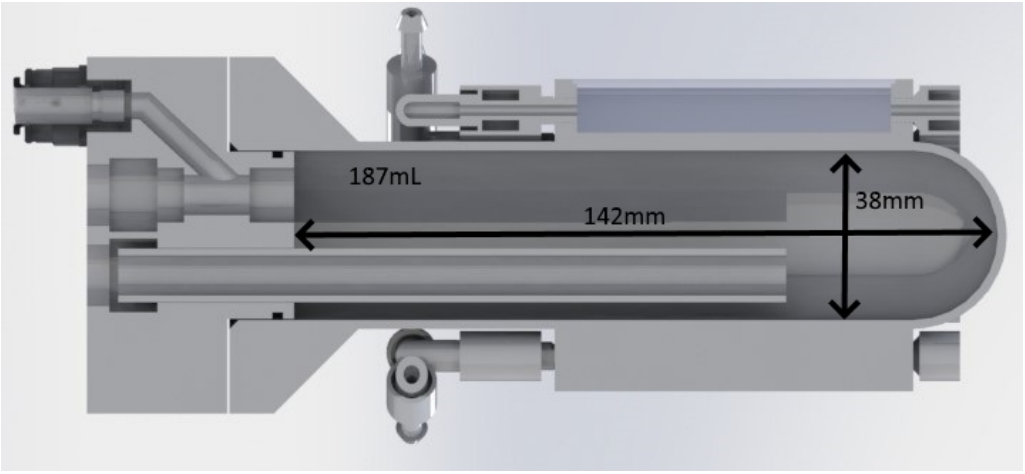

(c) Cross-section of the phantom. The inserted tube (bottom) ensures that the perfusate reaches the tip of the central cylinder (left ventricle) with limited recirculation. The outlet (top) has a side-branch that will ultimately connect to the myocardial chambers. Myocardial chambers can be seen on the outside of the left ventricle (right top and bottom). The myocardial chambers are either filled with a sponge or left empty. The dimensions are based on Lin et al. (2008) and Maceira et al. (2006). The ventricle is larger due to the Luer connectors.

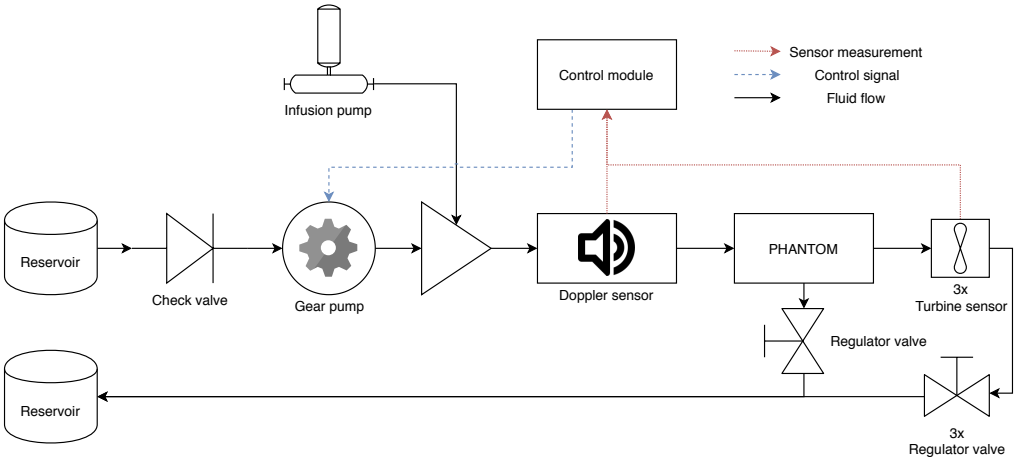

(d) Schematic overview of set-up. A check valve after the source reservoir prevents contaminated back-flow. A gear pump pumps the perfusate through the system. Tracer is injected before the flow feedback sensor (Doppler sensor). The perfusate then passes through the phantom where it separates into the aortic flow (downward) and the myocardial flow (right). The flow coming out each of the myocardial chambers is measured by turbine sensors. Each chamber and the aorta have a regulator valve that is used to tune the ratio between aorta and myocardium. The system is monitored and controlled by the control module.

Figure 4.3: Phase 1 phantom and set-up design based on an open-circuit configuration.

Myocardial chambers

Four phase 1 myocardial designs have been made. Version R1, figure 4.4a, is an empty chamber, with three inputs and outputs to distribute the flow. The lid is attached to the chamber via 6 screws. The second design, figure 4.4b, is a redesign of version R1 where the lid is glued on the chamber. The third design, figure 4.4c, opens on the front side instead of on the top. The fourth and final design, figure 4.4d, is a chamber with a 2^{nd} compartment. The flow passes through the tubes and can enter the myocardial chamber via holes. It is expected that the perfusate will circulate at a lower velocity and therefore stay longer in the myocardial chamber.

Version R1 does not have a fixed cap, adding to its flexibility. Different experiments can be performed, where the tissue mimicking material can be changed depending on the requirements. However, screws need material to create a thread which introduces certain dead-zones. Using glue to attach the cap, these dead-zones are removed and, simultaneously, acts as a seal.

The R2 design allows for a different kind of tissue-mimicking material, e.g. beads. Beads cannot be used in the R1 design since they cannot be properly stacked before falling out, which is not a problem in a front-opening design. The cap will be attached using glue to prevent dead-zones and to create a strong connection since there is too little space for a proper screw connection.

The R3 design aims to add a 2^{nd} compartment. Perfusate can exit the main tubes via a series of small holes where it will tend to circulate at a lower velocity. This design will be ideal to combine with a membrane that will trap the tracer once it exits the main tubes.

4.1.2 Simulation

Solidworks Flow Simulation is a simplified environment, which can simulate fluid flow with minimum inputs. It allows for an indication of the fluid's behaviour in a model and can be used to determine the effects of the R3 design. The simulation requires the input volume flow, which, for the myocardium, is assumed to be 100 mL/min, and the environmental pressure at the output, which is assumed to be atmospheric pressure of 101 325 Pa. The outcome of the SolidWorks simulation is only taken as an *indication* to evaluate the model's improvements.

The comparison is shown in figures 4.4f and 4.4g. The R3 design has a significant lower, up to a factor of 7, flow velocity in the chamber itself. Theoretically, this should increase the time tracer is in the chamber and thus effectively mimic trapping behaviour for a period of time.

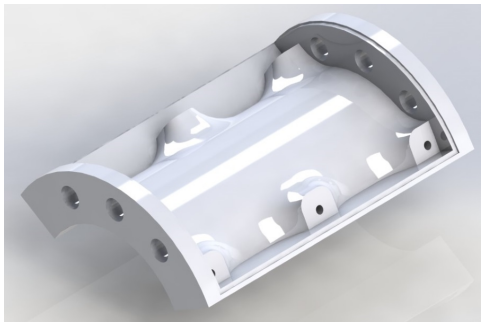

(a) Version R1. The cap is attached onto the chamber using screws.

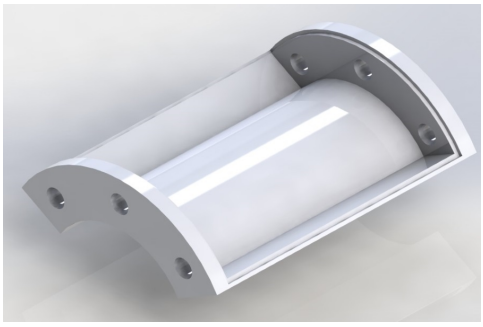

(b) Version R1.5. The cap is glued onto the chamber.

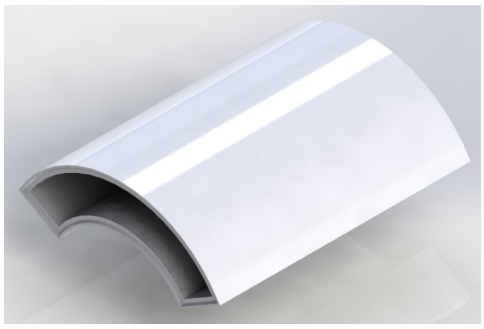

(c) Version R2. This design opens on the front side. It can be filled with "loose"-type of tissue mimicking materials, e.g. beads.

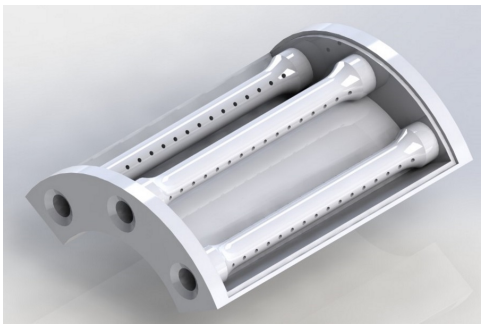

(d) Version R3. Tracer can exit the holed-tubes. The outflux of tracer is delayed compared to R1 and R2.

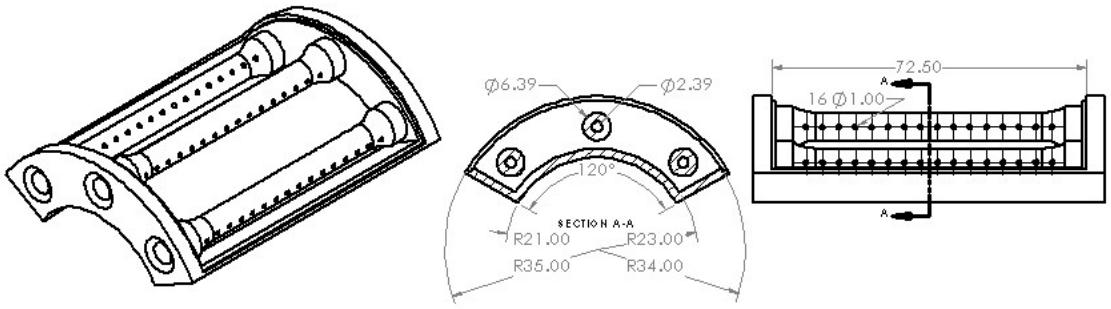

(e) Dimensional drawing of version R3. Physical dimensions are equivalent across designs. Additional dimensions for R3's tubes are given. The dimensions are based on Lin et al. (2008) and Maceira et al. (2006). Dimensions are in [mm].

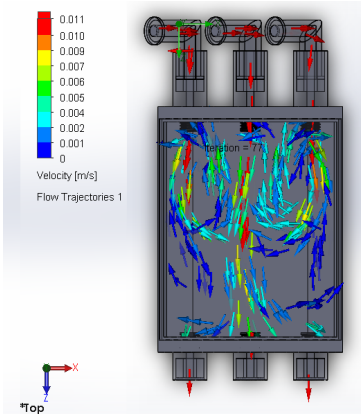

(f) Flow simulation of version R1 in SolidWorks. The perfusate circulates inside the chamber, delaying the outflow of tracer.

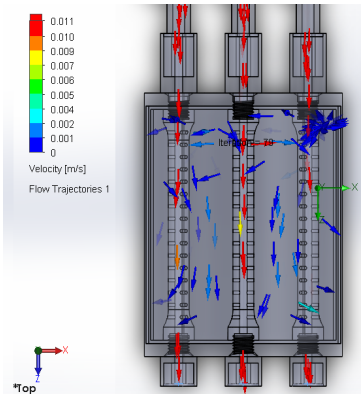

(g) Flow simulation of version R3 in SolidWorks. The velocity of the perfusate is approximately 7 times lower than the R1 design. More activity will thus be measured in the chamber.

Figure 4.4: Phase 1 chamber designs and simulations. Each chamber can be filled with tissue mimicking material.

4.1.3 Phase 2

The results from the first experiments, see section 5.1, showed that the phantom had poor symmetry; not all chambers were homogeneously filled. The side branch, must split repeatedly until there are 9 separate branches such that each myocardial chamber has three inputs for better distribution. Each split is realised by a "Y"-junction. The non-symmetry is caused by the uneven number of splits and the difference between branch lengths. The phase 2 cap, shown in figure 4.5a, aims to improve the symmetry and increase the tracer distribution in the myocardial chambers. After the design was printed, it proved difficult to clear the tracks of support material, which is necessary to print the tracks. Although the tracks were eventually cleared, a redesign is made without 90 degree angles for easier removal of the support material, see figure 4.5b. It is possible that some of the tracks become more biased due to the fluid's momentum.

The redesigned ventricle cap's right track series is somewhat more complex than the others. It can not reach the mantle on the right side without crossing the left ventricle's inlet. The tracks go around the inlet, increasing the track length. Tubes are still necessary to connect the ventricle with the myocardial chambers. Additionally, these tubes are required to simulate stenotic or blocked arteries using hose clamps or surgical clamps. The alignment of the connectors on the cap and myocardial chambers prevent a "spider-web". The relatively short distance and primarily horizontal orientation of the phantom should minimise the influence of gravity.

The phase 2 phantom itself, is shown in figure 4.6, and is slightly larger than an adult's heart. The printed tracks inside the myocardial chambers, the shortened left ventricle, and redundant Luer elbows should make the phantom more stable and more reliable. In addition, the included apex should make the phantom more compatible to patient studies.

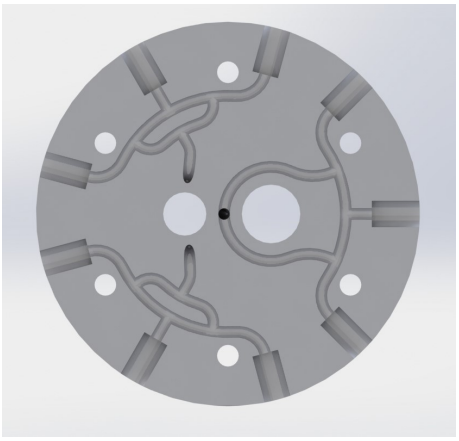

(a) Left ventricle cap version 2.

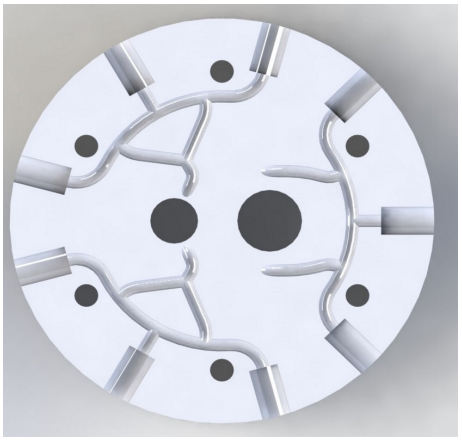

(b) Left ventricle cap version 3.

Figure 4.5: Ventrical cap designs. The outer most holes are clearance holes for screws such that the cap can be attached to the left ventricle. The ventricle inlet is the right central (larger) through hole, and the left ventricle outlet is the left central (smaller) through hole. The tracks originate from the outlet and end at the cylinder's mantle. The positions are aligned with the inlets of the myocardial chambers.

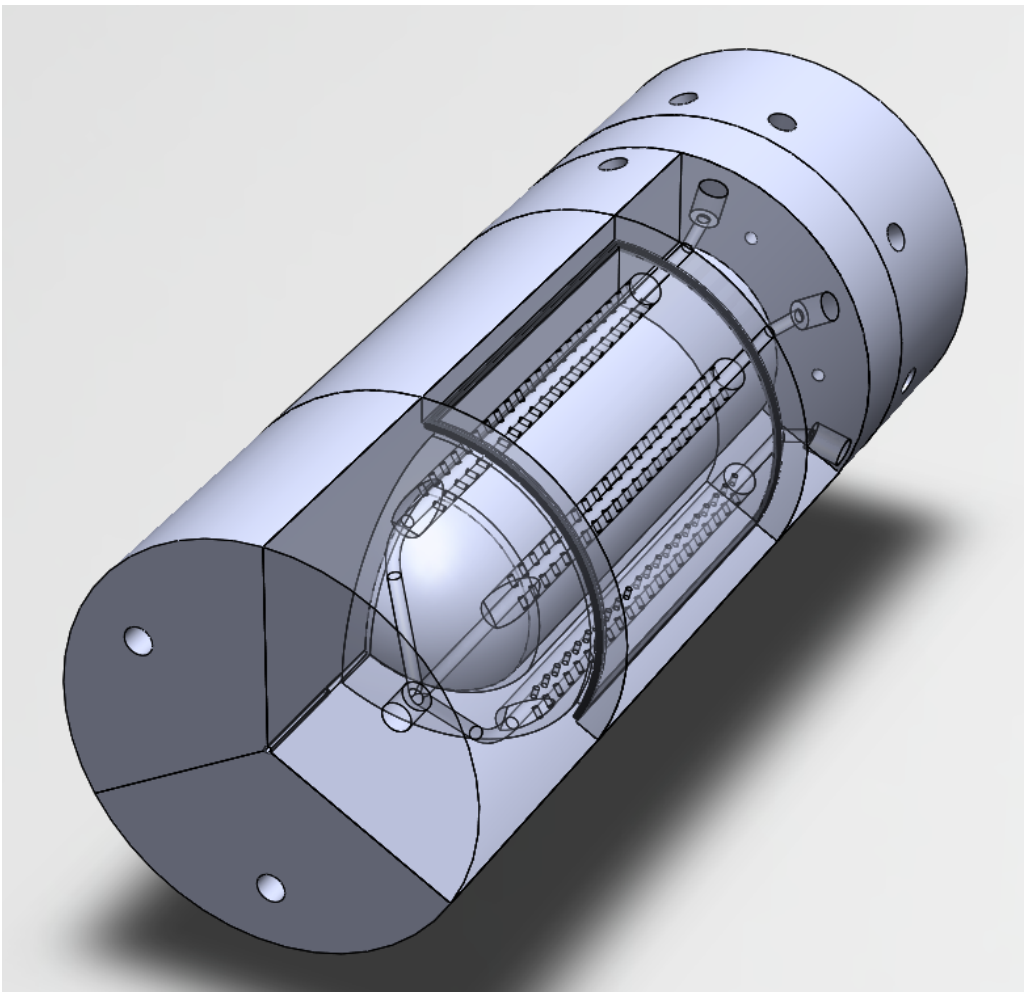

Figure 4.6: Phase 2 phantom design. The chambers are based on the R3 design. An apex, equally divided amongst the three chambers, is added to the R3 design. In addition, the chambers have printed input/output channels to remove the Luer elbow connectors and to combine the three output channels, reducing the size of the left ventricle. The left ventricle is approximately 40mm shorter than the phase 1 design.

4.2 Digital filter

During experiments in the individual assignment, significant noise artefacts appeared on the measured signal; white and impulse noise. The white noise is generated by all kinds of interference sources, e.g. power outlets, phone signals, WiFi, whereas the impulse noise is generated specifically by fast switching currents, e.g. switching of a relay, PWM signal to the pumps. The primary white noise source is, due to the 100Hz sampling rate, power outlets (Dutch standard is 50Hz).

Both noise types have one thing in common: relative high-frequency components. A low-pass filter is thus required. High order filters have better amplitude and frequency responses but can become CPU intensive. Therefore, only low order and IIR filters are taken into account. The ideal digital filter, for this project, maximises the attenuation at high frequencies while maintaining low attenuation at the lower frequencies.

Two simple digital filters, figure 4.7, have been evaluated: an average filter (equation 4.1), with different weights, and a Butterworth filter (equation 4.2), with different corner frequencies. A Butterworth filter has been chosen because of its flat characteristic (Butterworth filter is also called a maximally flat magnitude filter), its simpler calculations and more linear phase response at low orders than other filters, e.g. Chebychev, Bessel, elliptic (Kumar, 2016), and the average filters. A first order Butterworth filter is used to prevent a non-linear phase response.

$$y[n] = \frac{Z-1}{Z} \cdot y[n-1] + \frac{1}{Z} \cdot x[n] \tag{4.1}$$

$$y[n] = -\sum_{k=1}^{N} a_k y[n-k] + \sum_{k=0}^{N} b_k x[n-k] \tag{4.2}$$

Where:

n = current sample number,
$y[n]$ = current output value,
$x[n]$ = current sensor value,
Z = filter weight,
k = index,
a_k = Butterworth approximated output coefficient,
b_k = Butterworth approximated input coefficient,
N = Filter order, 1.

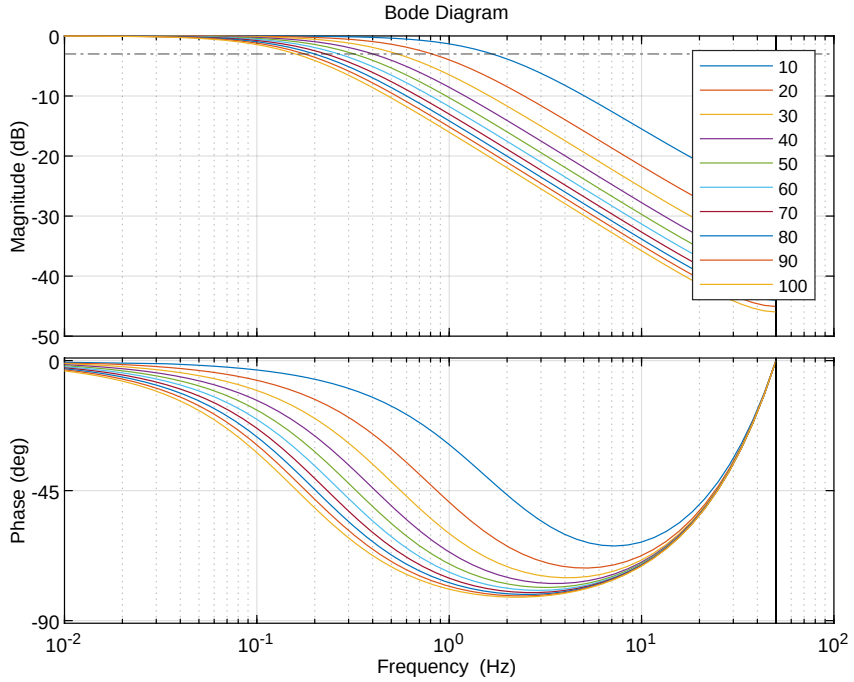

(a) Average filters with different weights (Z), varying between 10 and 100.

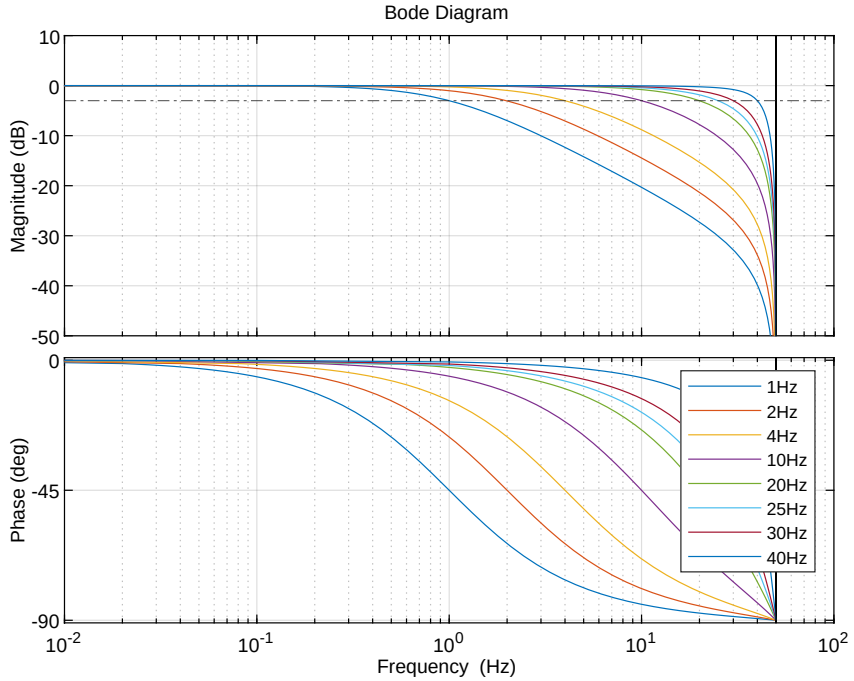

(b) (Shifted) Butterworth filters with different corner frequencies, varying between 1 and 40 Hz.

Figure 4.7: Average and Butterworth low pass filters.

4.3 GUI

The new, and improved, GUI, is shown in figure 4.8. It looks similar to the old MATLAB GUI, also called a MATLAB app, developed in the individual assignment of Gijs de Vries. The MATLAB app has been made in a relatively short time and contained numerous bugs. These bugs, and some design choices, resulted in an GUI that cannot be used as a stand-alone application without an internet connection. The new GUI is developed in Qt (pronounced "cute") and uses C++. The code can be deployed as an executable without any dependencies on external programs. In addition, extra functionality is implemented to make the GUI more intuitive:

- COM-port selection window,
  Seperate window that lists all available COM-ports. Extra information is shown on the selected port such that the correct port can be chosen.
- Automatic COM-port checking,
  Before and after a COM-port is selected, the validity is verified on a timer. If the port is no longer valid, it is removed or unselected.
- Horizontal zooming,
  A slider in the GUI allows the user to see older data (up to 60 seconds with a resolution 10Hz).
- Automatic zooming.
  The vertical limits are automatically set (when enabled) depending the horizontal slider.

The GUI consists of different areas, each with a certain function:

1. Analogue sensor parameters,
   Each tab corresponds to a different analogue sensor. After enabling a sensor, the user can enter the slope and elevation parameters. The sensor type can be switched between flow or pressure, where the input units automatically adjust accordingly. The drop-down menus allows the user to enter the sensor's parameters in the units mentioned in the sensor's data-sheet.
2. Digital sensor parameters,
   Each tab corresponds to a different digital sensor. After enabling a sensor, the user can enter the sensor's output in pulses per measured unit. The sensor type can be switched between flow or pressure, where the input units automatically adjust accordingly. The drop-down menu allows the user to enter the sensor's parameters in the units mentioned in the sensor's data-sheet.
3. Pump parameters,
   Each tab corresponds to a different pump. As of Wednesday 10^{th} July, 2019, only the first two pumps are connected in the control module. After enabling a pump, the user can enter the flow rate and select the feedback sensor. The feedback sensor must be a valid flow sensor previously enabled in areas 1 and/or 2. The drop-down menu is automatically filled, or emptied according to enabled flow sensors. When the system is operational, the user can press the "Update pump rate"-button to change the desired flow rate.
4. COM-port,
   By pressing the "Select COM-port"-button, a pop-up window appears that allows the user to select a port from the automatically refreshed drop-down menu. The user sees extra information on the selected COM-port to ensure he/she selects the proper port. The selection must then be confirmed and the status is then showed in the main window of the GUI. The status is automatically updated based on the availability of the port.
5. Output file,
   The user can enter a custom name in the "File name"-field. The default value is "sensorData". The CSV file is created when the "Record experiment" is pressed and the file name is always preceded by the date and time (YYYYMMDD_HHMMSS-format). The "Rename last"-button allows the user to rename the last output file.

6. Main controls,
   The "Initialise set-up"-button is the dedicated start-button. The "Record experiment" starts the recording of the sensor measurements to a specified file. Any status updates on the system (wrong inputs, errors) are shown next to the buttons.

7. Sensor selection,
   Sensors that are enabled in areas 1 and/or 2, are automatically checked. Checked sensors are plotted in areas 9 or 10. By un-checking certain sensors, the data will not be shown in the graphs but will still be recorded.

8. Limit selection,
   The horizontal limit can be manually adjusted by dragging the slider to the left or right. The further the slider is to the left, the more data is shown, up to 60 seconds in the past. The vertical limits can manually be set by un-checking the tick-box and inputting the axis' limits.

9. Flow graph,
   The left graph shows the system's measured flow rates on a 10Hz refresh rate. The measurement are received and written to the output file at 100Hz.

10. Pressure graph,
    The right graph shows the system's measured pressures on a 10Hz refresh rate. The measurements are received and written to the output file at 100Hz.

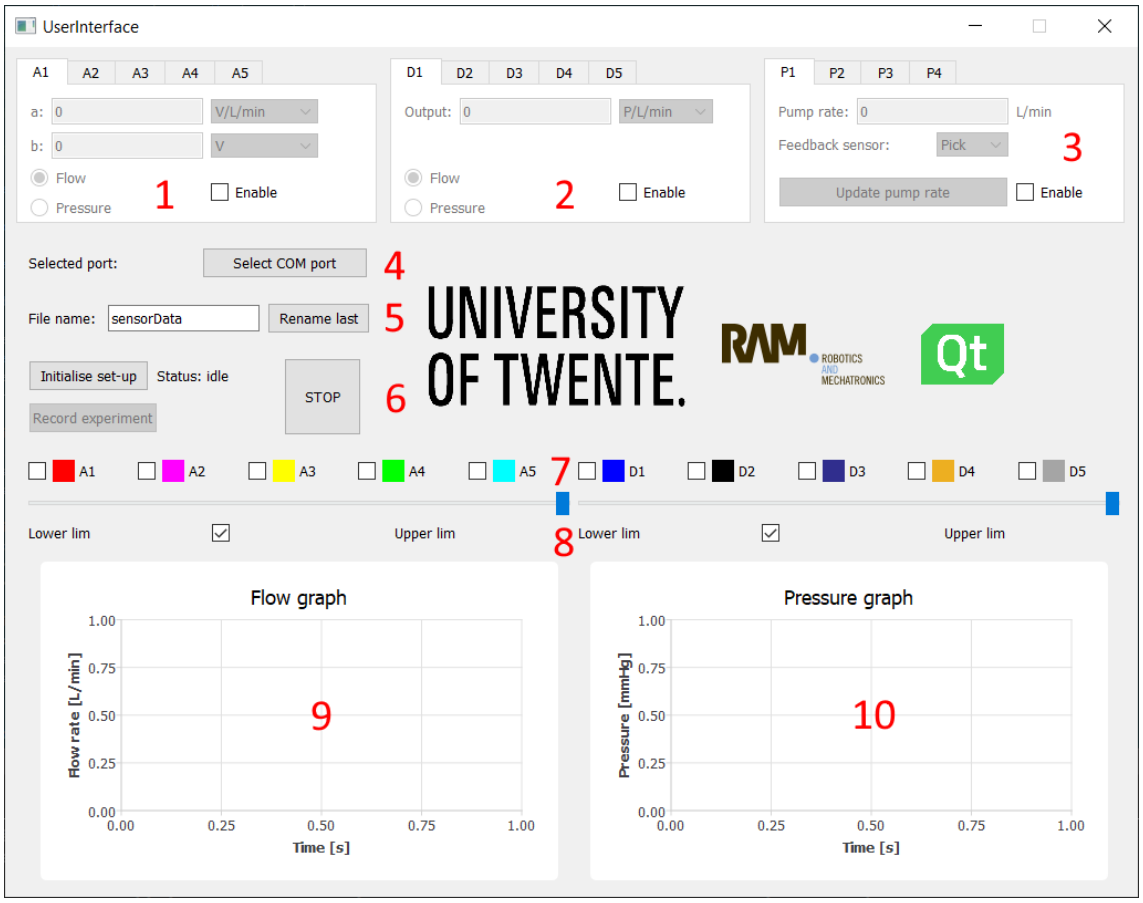

Figure 4.8: Graphical User Interface.

5 Results

This chapter shows the results of each of the two main phases and the orientation experiment. The results of the two main phases are intensity images and the accuracies of the flow rates in the left ventricle and myocardial chambers.

5.1 Phase 1

The results of the first phase are shown in figure 5.1. The global TAC, figure 5.1a, and the perfusion TAC, figure 5.1b, show a singular, high peak corresponding to the left ventricle (and thus the AIF) and a lower myocardial peak.

The cross-sectional intensity images, figures 5.1c and 5.1d, show that the phantom is recognised by 4DM as a normal heart. It can clearly be seen that the left ventricle chamber is filled properly and a reliable AIF can be retrieved by drawing an ROI in the ventricle. However, the perfusion in the myocardial chambers is non-homogeneous. The accuracy of the measurements is shown in table 5.1.

Table 5.1: Accuracy results of the flow set-up. The percentages are relative to the average flow value. The average itself is not relevant since it varies between experiments.

Date		Aorta [%]	LCx [%]	LAD [%]	RCA [%]	Note
18/04/2019 (2 experiments)	**sigma**:	0.355	0.925	N/A	N/A	
	Max:	1.065	2.615	N/A	N/A	1 sensor available
	Min:	1.12	1.255	N/A	N/A	
25/04/2019 (3 experiments)	**sigma**:	0.88	1.353	N/A	N/A	
	Max:	1.66	5.357	N/A	N/A	1 sensor available
	Min:	2.41	2.700	N/A	N/A	
02/05/2019 (3 experiments)	**sigma**:	0.473	6.820	3.227	6.677	
	Max:	0.963	24.803	10.653	19.417	
	Min:	1.143	10.090	7.527	14.427	

5.2 Orientation experiments

The orientation have been determined to be approximately 0° (or 360°) for the VLA slice (top left angle in figures 5.2a and 5.2b), and approximately 90° for the HLA slice (top right angle in figures 5.2a and 5.2b).

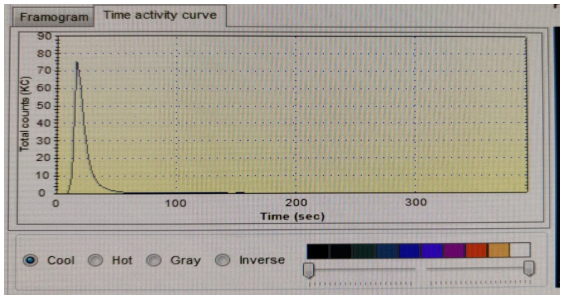

(a) Global TAC. The Y-axes is the activity throughout the entire image over time.

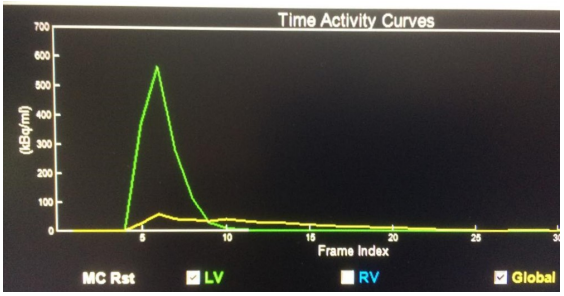

(b) Perfusion TAC. The Y-axes is the activity in the phantom. The high peak is the the activity in the left ventricle (AIF), while the yellow line is the average activity in the myocardial chambers. The X-axes are the frame indices, first 20 frames every 3 seconds and the remainder are every 30 seconds.

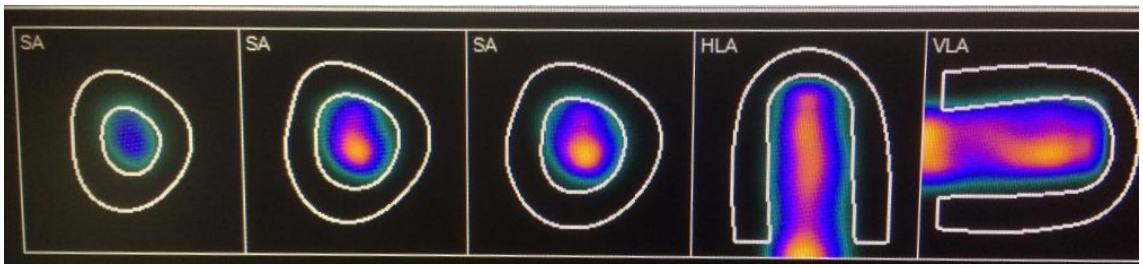

(c) AIF cross-sectional intensity images. It can clearly be seen that the left ventricle is filled with tracer. The colours are relative, blue is less activity than the orange/white colours. If the image is in black/white, the brighter areas have a higher activity.

(d) Myocardial cross-sectional intensity images. It can clearly be seen that some myocardial chambers have relatively more activity, brighter colours, than others. The tracer is not homogeneously divided.

Figure 5.1: Phase 1 results.

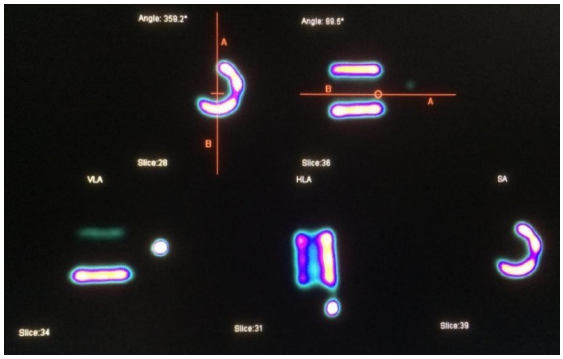

(a) $2/3^{rd}$, statically filled myocardium. This experiment is performed to determine the angles in the 4DM software. The empty myocardial chamber is not filled with tracer and thus shows no activity. The dot shown in the bottom left image represents the apex.

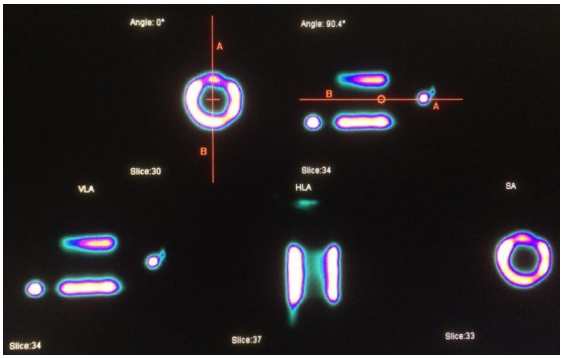

(b) Fully filled myocardium. This experiment is used to determine the phantom's cross-sectional images in the perfect situation: all chambers homogeneously filled. The same angles are used from figure 5.2a.

Figure 5.2: Orientation experiment results.

5.3 Phase 2

The results of the first phase 2 experiment are shown in figures 5.3a to 5.3c. The AIF is a single high peak of similar height as clinical AIFs. The myocardial TACs are significantly lower than those found in patients.

The AIF intensity image, 5.3b, shows that the tracer fills the left ventricle of the phantom and a reliable AIF can be taken. The myocardial chambers, see figure 5.3c show some activity which is not homogeneously distributed. It can be seen that the apex has some activity.

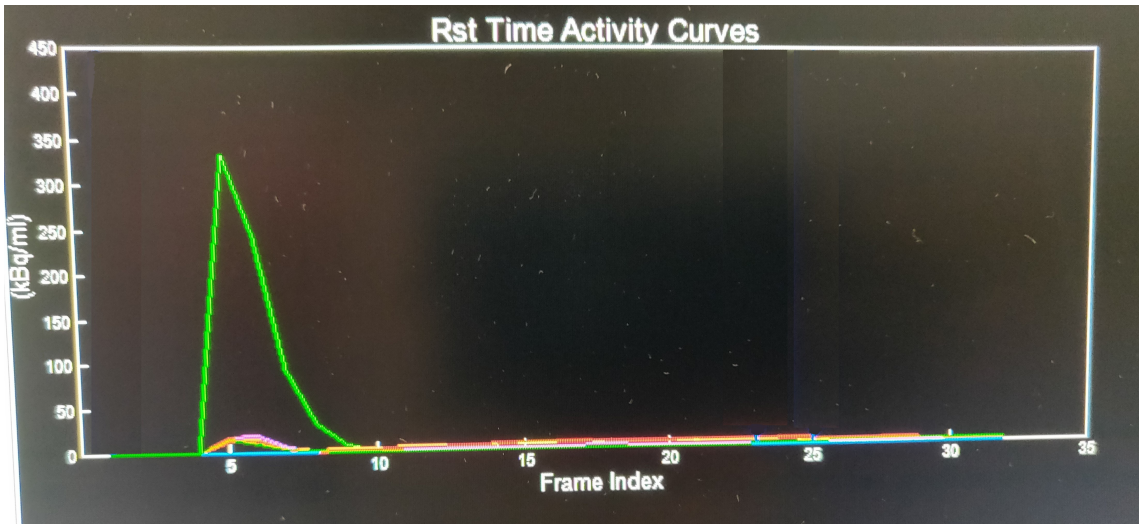

(a) Phantom's TAC. The large peak (green line) is the AIF, the smaller peaks (other coloured lines) are for the myocardial chambers. The myocardial intensity curves are relatively low and do not have a steady offset.

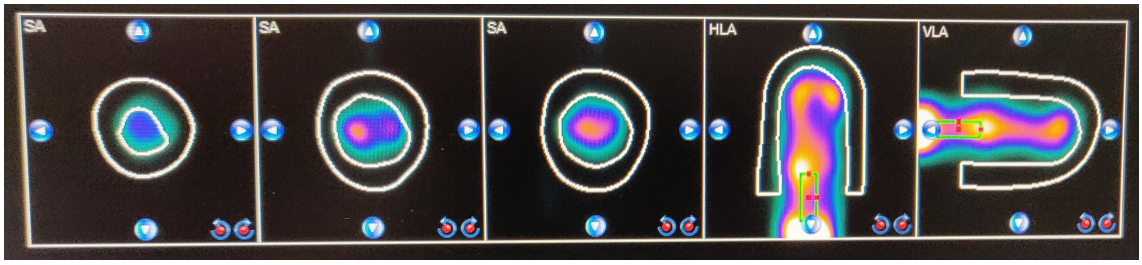

(b) AIF cross-sectional intensity images. It can clearly be seen that the left ventricle is filled with tracer. The colours are relative. Blue is less activity than the orange/white colours. If the image is in black/white, the brighter areas have a higher activity.

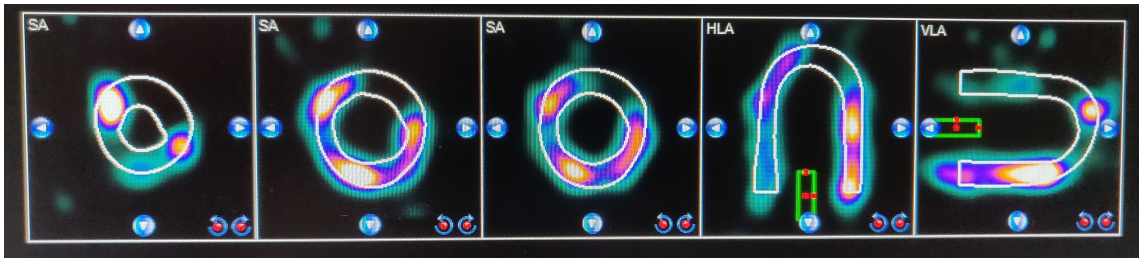

(c) Myocardial cross-sectional intensity images. It can clearly be seen that some myocardial chambers have relatively more activity, brighter colours, than others. The tracer is not homogeneously divided. However, from the two right-most images, it can be seen that the apex has some activity.

Figure 5.3: Phase 2, first experiment, results.

The results of the second phase 2 experiment are shown in figures 5.4a to 5.4c. The AIF is a single high peak, slightly lower than a clinical stress AIF. The myocardial TACs are significantly lower than those found in patients.

The AIF intensity image, 5.4b, shows that the tracer fills the left ventricle of the phantom and a reliable AIF can be taken. The myocardial chambers, see figure 5.3c show more activity than the first experiment but is not homogeneously distributed. The apex is clearly visible.

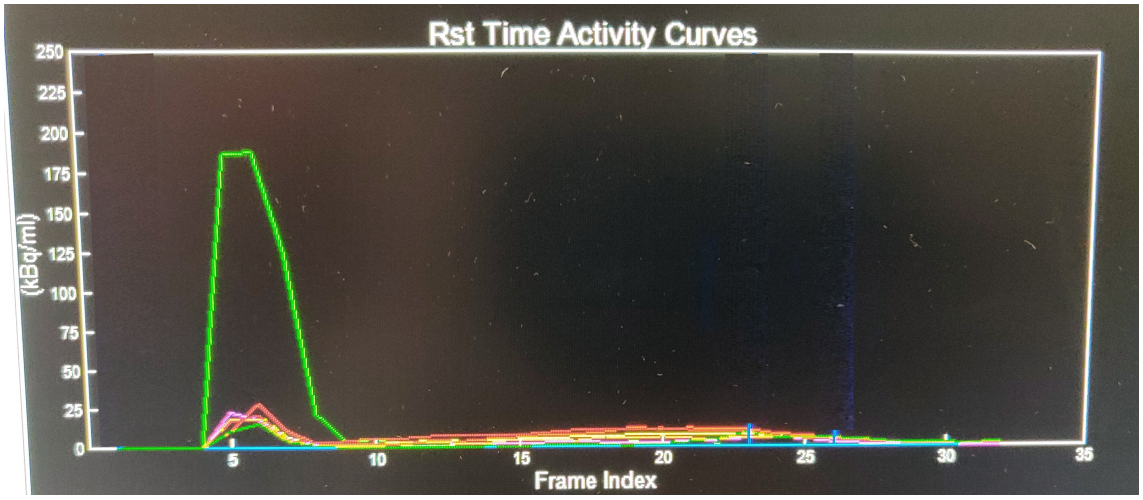

(a) Phantom's TAC. The green line is the AIF, the other coloured lines are for the myocardial chambers. The myocardial intensity curves are relatively low and do not have a steady offset. The flattened peak is caused by the activity being divided among two frames instead of one. The peak height is lower than the other AIFs, making the area under the curve similar.

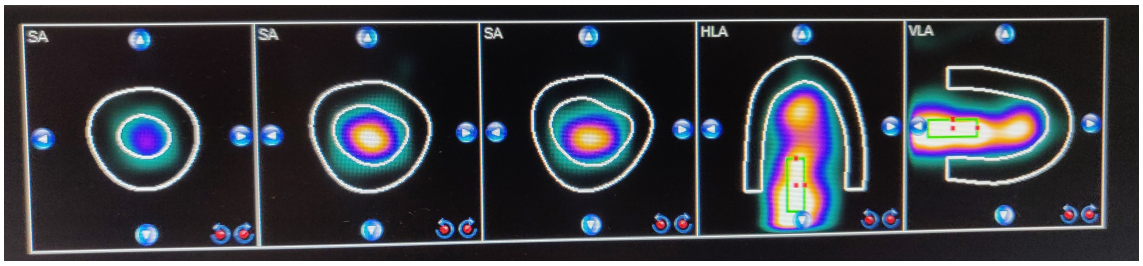

(b) AIF cross-sectional intensity images. It can clearly be seen that the left ventricle is filled with tracer. The colours are relative. Blue is less activity than the orange/white colours. If the image is in black/white, the brighter areas have a higher activity.

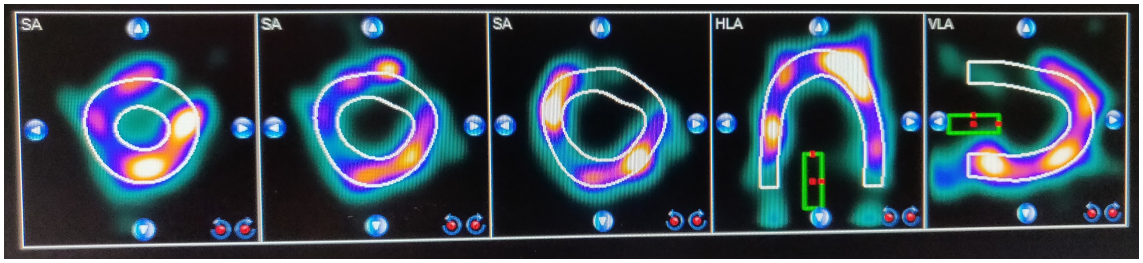

(c) Myocardial cross-sectional intensity images. It can clearly be seen that some myocardial chambers have relatively more activity, brighter colours, than others. The tracer is not homogeneously divided. However, from the two right-most images, it can be seen that the apex has a good distributed activity.

Figure 5.4: Phase 2, second experiment, results.

The results of the third phase 2 experiments are shown in figure 5.5. The AIF is a single large peak of the same height as a clinical AIF. The tracer in the left ventricle itself shows good distribution, see figure 5.5b. The myocardium, see figure 5.5c, shows a non-homogeneous distribution of the tracer throughout the chamber, and some activity can be seen in the apex.

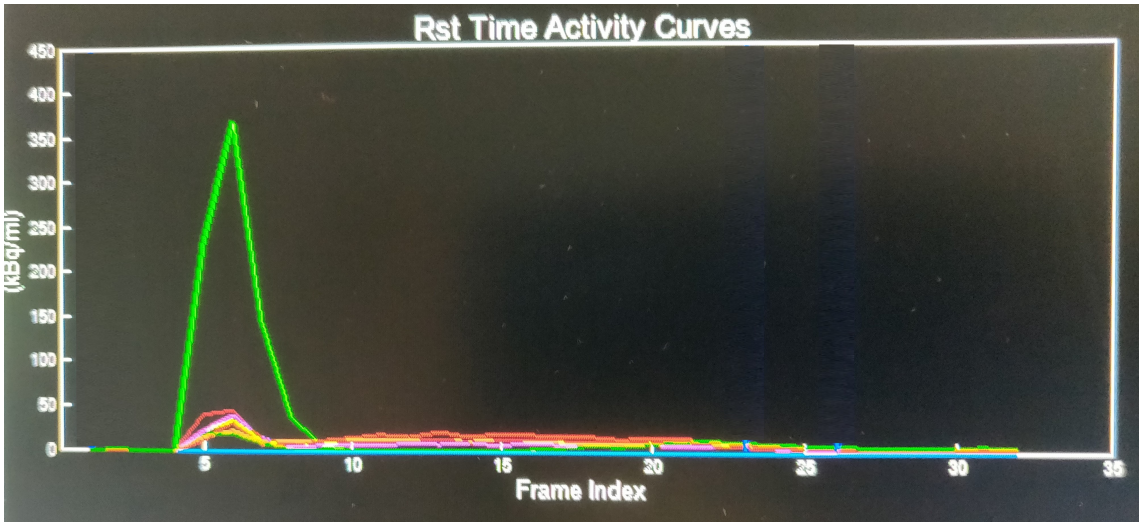

(a) Phantom's TAC. The green line is the AIF, the other coloured lines are for the myocardial chambers. The myocardial intensity curves are relatively low and do not have a steady offset.

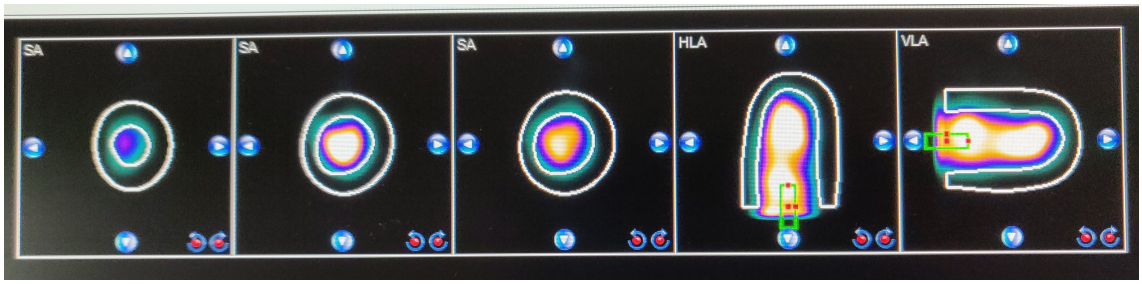

(b) AIF cross-sectional intensity images. It can clearly be seen that the left ventricle is filled with tracer. The colours are relative. Blue is less activity than the orange/white colours. If the image is in black/white, the brighter areas have a higher activity.

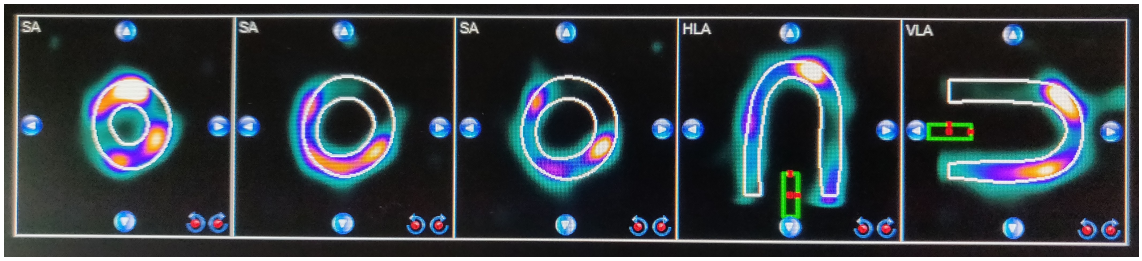

(c) Myocardial cross-sectional intensity images. It can clearly be seen that some myocardial chambers have relatively more activity, brighter colours, than others. The tracer is not homogeneously divided. However, from the two right-most images, it can be seen that the apex has some activity.

Figure 5.5: Phase 2, third experiment, results.

The results of the fourth phase 2 experiments are shown in figure 5.5. The AIF is a single large peak (green line) of the same height as a clinical AIF. The tracer in the left ventricle itself shows a good distribution, see figure 5.5b. The myocardium, see figure 5.5c, shows a non-homogeneous distribution of the tracer throughout the chamber, and an accumulation of tracer can be seen in the apex.

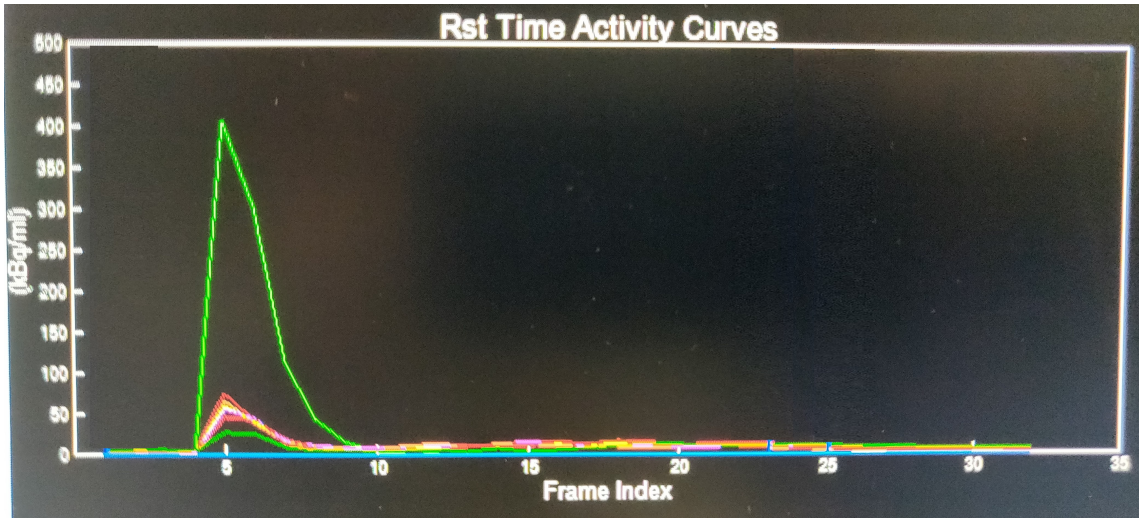

(a) Phantom's TAC. The green line is the AIF, the other coloured lines are for the myocardial chambers. The myocardial intensity curves are relatively low and do not have a steady offset.

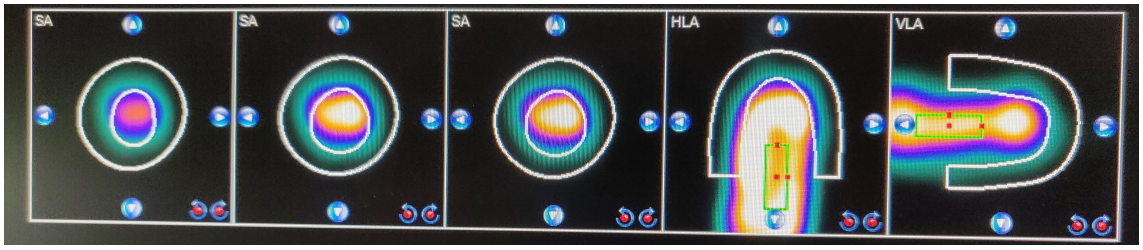

(b) AIF cross-sectional intensity images. It can clearly be seen that the left ventricle is filled with tracer. The colours are relative, blue is less activity than the orange/white colours. If the image is in black/white, the brighter areas have a higher activity.

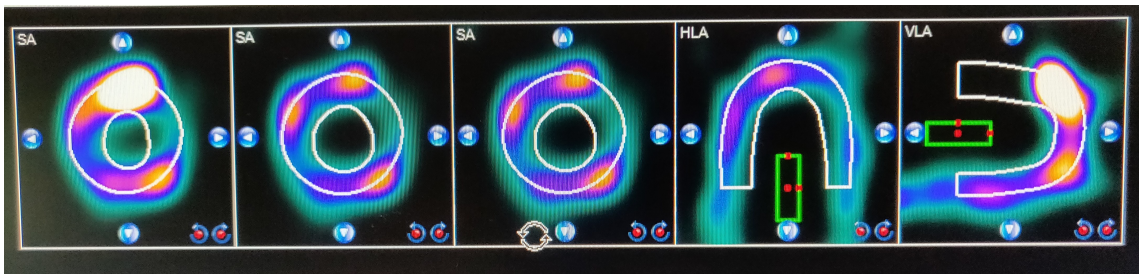

(c) Myocardial cross-sectional intensity images. It can clearly be seen that some myocardial chambers have relatively more activity, brighter colours, than others. The tracer is not homogeneously divided. However, from the two right-most images, it can be seen that the apex has some activity.

Figure 5.6: Phase 2, fourth experiment, results.

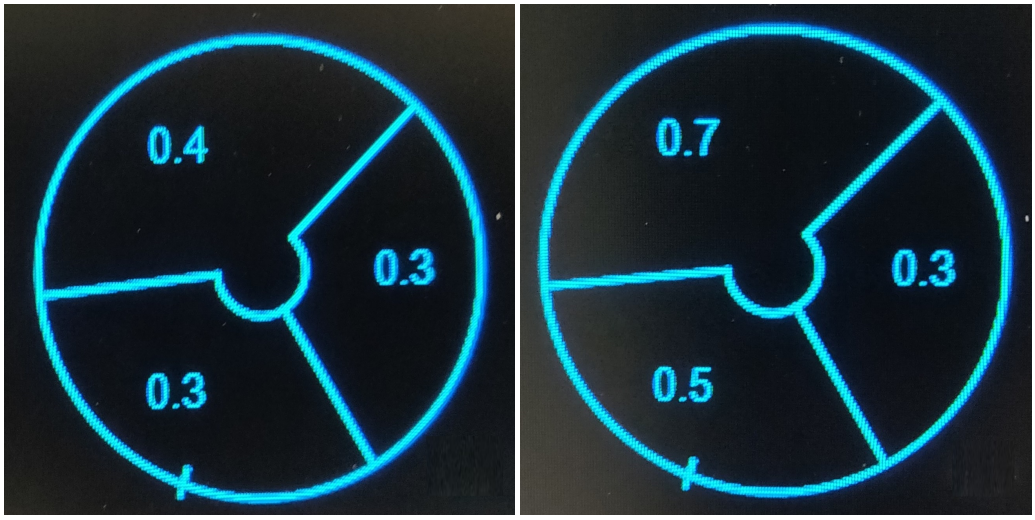

(a) Third experiment's myocardial perfusion rate, in mL/min/g, for each of the three myocardial chambers, as calculated by 4DM.

(b) Fourth experiment's myocardial perfusion rate, in mL/min/g, for each of the three myocardial chambers, as calculated by 4DM.

Figure 5.7: The comparison between the third (left) and the fourth (right) experiment's calculated perfusion rates. Both experiments have been performed using the same set-up with the same parameters.

The accuracy results of phase 2 are shown in table 5.2. The experiments have been experiencing noise on the myocardial sensors resulting in large deviations of the average flow. During some experiments, the sensor's signal was lost entirely.

Table 5.2: Phase 2 accuracy results of the flow set-up. The percentages are relative to the average flow value. The average itself is not relevant since it varies between experiments.

Date		Aorta [%]	LCx [%]	LAD [%]	RCA [%]	Note
02/07/2019 (2 experiments)	**sigma**:	0.296	36.023*/**	6.108**	7.178	*Sensor data contained large noise spikes.
	Max:	0.863	116.389*/**	12.046**	22.397	**Based on only 1 of the 2 sensors.
	Min:	1.455	51.898*/**	10.148**	14.013	
04/07/2019 (3 experiments)	**sigma**:	0.590	177.941*	108.012*	10.025*	*Sensor data contained large noise spikes.
	Max:	1.957	1082.164*	752.030*	44.357*	*Based on only 2 of the 3 sensors.
	Min:	0.93254	69.6648*	39.185*	24.927*	

This page is intentionally left blank.

6 Discussion

This chapter discusses the outcome of both main phases and the orientation experiments. The last section compares the outcome to the research questions stated in the beginning of this thesis.

6.1 Phase 1

The initial results show that the phantom is recognised as a heart by 4DM; the outlines can be seen in figure 5.1. Nevertheless, the tracer has not been distributed equally despite simulating ideal perfusion. The AIF shows a single sharp peak and a ROI can be taken from within the ventricle. The myocardium, however, is not completely filled with tracer, which is likely to be caused by the side-branch. The side-branch splits into 9 distinct branches, three for each chamber, by using "Y"-connectors; it is not done symmetrically. Furthermore, two of the chambers are filled with different sponges to simulate tissue, while one chamber is kept empty.

The results of the experiments cannot be fully evaluated, especially the quantitative measurements, since the orientation in the software could not be determined. The rotational orientation cannot be determined since it is not possible to identify the chambers based on the images. Furthermore, the missing apex makes it difficult to determine the left and right orientation. An orientation experiment is planned before phase 2 experiments such that the proper angles can be determined and used to properly evaluate the experiments.

6.2 Orientation experiments

The angles that have been determined in the orientation experiment, 0° (or 360°) VLA and 90° HLA, can be used in every experiment. These angles correspond to a horizontal HLA (parallel to the flattened patient chair) and vertical VLA (perpendicular to the flattened patient chair), both relative to global coordinates rather than machine coordinates. Using these angles will ensures that the myocardial chambers are aligned with the vascular model, see figure 6.1. It can be seen that the brighter areas fit in the RCA and LCx regions. The LAD region is not properly filled, because the tracer has not been properly distributed inside the chamber; it remained near the injection point. Initial mixing can be seen by the darker blue near the top of the perfusion model. In addition, it can be seen, by the transition in colours, that the physical chambers have the same orientation as the software model; blue colour is on the edges of the LCx, RCa, and LAD regions.

6.3 Phase 2

The primary focus of the second phase, is to test the phantom's unique design. The results show that the tracer enters the phantom and reaches the apex, resulting in the characteristic horseshoe shape in the VLA and HLA. Precautions had been taken to prevent air from entering the phantom between experiments: submerged pump, check-valve after pump, valve on the outlet of the left ventricle, a simple water-trap, and anti-siphoning valves. However, it still showed large non-perfused areas. The non-perfused area are likely caused by (large) air bubbles, despite the precautions and the venting of the phantom before the first experiment. These bubbles can originate from the water itself, due to the mechanical interaction of the pump with the water, or that air flowed back in, in-between experiments. The speed in which air returns into the phantom has been reduced compared to initial experiments at the university, before these precautions had been implemented. However, as the results show, it has not completely solved the problem.

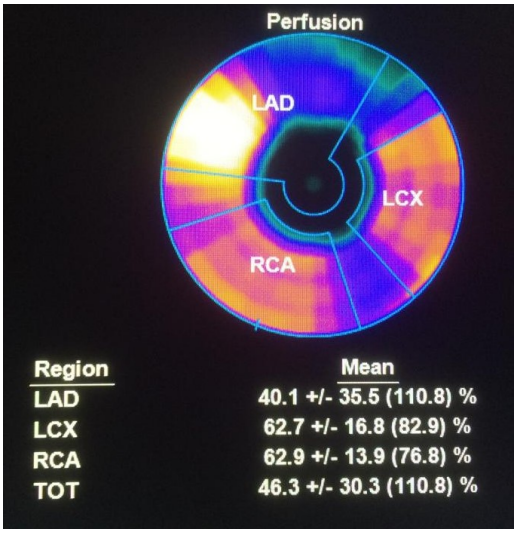

Figure 6.1: Orientation alignment of phantom. The RCA and LCX chambers have been homogeneously filled while the LAD chamber has not. The percentages show the area, within each region, that has been perfused, relative to the highest (brightest colour) perfusion (the bottom left part of the LAD region).

The first experiment of the day showed proper distribution of the tracer in the apex. However, the second experiment of the day showed the accumulation of the tracer. The holed-tubes in the myocardial chamber are straight through the chamber and do not curve around the apex (see figure 4.6). Therefore, there is no active circulation of the perfusate at the apex. Tracer that reaches the apex, for example through convection, is only removed through dilution. Dilution is a slow process at an area without active flow, whereas the tracer in the remainder of the chamber is removed more quickly due to the active flow. Since the tracer is only "trapped" in the apex, the calculations for the perfusion, by 4DM, are unreliable. The calculated perfusion rate differs between experiments where no changes have been made to the set-up and its parameters, see figure 5.7.

The phase 2 measurements show significantly more noise in the measurements compared to the phase 1 results, see tables 5.2 and 5.1 respectfully. No changes have been made to the control module between experiments performed on 2 May and 2/4 July. Likely reasons are external noise and noise by the power supplies/motor controller. External noise is minimised by the shielded case of the control module, and decoupling, using optic couplings, of the sensor inputs. However, inside the control module, an unshielded transformer reduces the AC-input (230VAC) to 22VAC and an unshielded motor controller switches a high current signal for the pump. Both of which can introduce significant noise on the measurements.

6.4 Evaluation

Three sub-research questions have been established at the beginning of the project. This section refers back to these research questions and compares it to the results of the previous chapters. The last part of this section refers back to the main research question.

What are the main requirements that the phantom must meet?

The phantom is designed to meet five primary requirements:

- Be compatible with clinical software;
- Have a system-based Arterial Input Function with coupled myocardial Time-Activity Curves, which are equivalent to clinical practice;
- Be of comparable physical size;
- Model a 2^{nd} compartment;
- Have the ability to simulate defects in an anatomical manner.

The phase 2 phantom is compatible with clinical software, has a comparable system-based AIF with coupled myocardial TAC, tries to model a simplified 2^{nd} compartment, and is able to simulate defects in an anatomically by clamping flexible tubing. However, tracer is not trapped in the phantom, and therefore does not model a true 2-compartment model. Futhermore, it's physical size is slightly larger than the heart of an average adult.

What perfusion phantoms do already exist and are they suitable?

Several phantoms, for different modalities, have been evaluated. Two of the phantoms showed interesting characteristics. Both phantoms had a SA slice of a circle, but missed an apex. One of these two phantoms missed an AIF altogether, while the other had a programmable AIF. None of the phantoms, including the two previously mentioned, are directly compatible with clinical software. Modifications are required to the clinical software, or their own software had to be used. Therefore, these phantoms cannot, reliably, be used to validate the quantitative measurements.

How can the phantom meet the clinical requirements and mimic the perfusion of a human heart?

The phantom meets the clinical requirements by having a centralised left ventricle with a surrounding myocardium. The AIF can be retrieved from the left ventricle and the myocardial TACs are coupled to the AIF by a branching aorta, as it is in a human heart. The phase 2 phantom does not trap the tracer, it delays it. The phantom does not mimic a true 2-compartment model. However, with additional development, by adding tissue mimicking material, it can simulate a true 2-compartment model. Additionally, the tracer accumulates in the apex causing the 4DM software to misinterpret the myocardium, interfering with the perfusion calculations, and rendering the outcome unreliable for validation purpose.

Can patient treatment reliably depend on the D-SPECT, using dynamic scanning, in myocardial perfusion imaging?

The main research question guided the project, but has not been the primary goal. Further data acquisition and analysis is required to answer the main research question. In addition, in its current state, the phantom is not yet suitable to validate the D-SPECTS quantitative measurements.

The phantom's image, in 4DM, is equivalent to image of the heart of an average adult; a left ventricle with surrounding myocardium. The myocardial perfusion is simulated similar to physiological perfusion. Water (with tracer) enters the left ventricle, where an AIF can be determined, and exits through an aorta. The flow to the myocardium originates from side branches of the aorta, ensuring a coupled myocardial TAC. These characteristics make the phantom unique since it is directly compatible with clinical software. However, it is required to improve and optimise the phantom and its set-up. The phantom does not have a true second compartment and the measurements, taken with the control module, have a low Signal-to-Noise Ratio.

7 Conclusion

This chapter concludes both main phases and the orientation experiment. The end of this chapter refers back to the main research question.

7.1 Phase 1

The primary goal of the first phase, is to develop a proof-of-concept phantom to demonstrate that the phantom is compatible with clinical software. The results of the first phase, although not ideal, show that the modular perfusion phantom can be used in conjunction with the 4DM clinical software. The phantom meets the remainder of the requirements. However, since it delays the tracer instead of trapping it, the phantom does not model a true 2-compartment model. Furthermore, the tracer is not distributed equally among the three myocardial chambers and thereby mimics a defect while ideal perfusion had been the goal. This shows that a more symmetrical design is needed to distribute the tracer equally.

7.2 Orientation experiments

The primary goal of the orientation experiments has been to find the orientation angles used by 4DM which aligns the phantom with the software models. The experiments have been successful. The acquired angles can be used to align the software model with the physical phantom in any future experiment, ensuring that the physical measurements can be compared to 4DM's outcome.

7.3 Phase 2

Initial results showed that the phantom remained compatible with clinical software (4DM), and that the newly added apex is clearly visible. However, tracer accumulates in the apex, especially after the first experiment, and interferes with the perfusion calculations by 4DM. Furthermore, the measurements had a poor Signal-to-Noise Ratio, further decreasing the reliability of the perfusion phantom.

Can patient treatment reliably depend on the D-SPECT, using dynamic scanning, in myocardial perfusion imaging?

The primary goal of the project had been to develop the perfusion phantom, that is compatible with clinical software, for the purpose of validating the D-SPECT's quantitative measurements. In its current state, the phantom, and its set-up, cannot yet be used to validate the D-SPECT and to answer the main research question. However, the phantom's flow design is unique. It is the first phantom that is directly compatible with clinical practice and software.

With further development, the myocardial perfusion phantom, as described in this thesis, can be the corner stone for future phantom validation studies. Not only for the D-SPECT's quantitative measurements, but, potentially, also for other modalities.

8 Recommendations

The phantom, as described in this thesis, requires future development before it can, reliably, be used for the validation of the D-SPECT, and possibly other modalities. Two major flaws have been mentioned in chapter 6. This chapter describes points of improvements for the phantom, and its set-up.

8.1 Optimisation

The optimisation section consists of possible improvements primarily to the control module. The control module has been developed during the individual assignment of Gijs de Vries, and has therefore not been introduced in this thesis. However, it is important to mention possible improvements since the set-up depends on the control module.

Digital filter
The initial measurements, without a digital filter, showed significant noise. The digital Butterworth filter that has been implemented improved the Signal-to-Noise ratio. A low order Butterworth filter has been chosen due to its flat spectrum and linear phase response. A higher order filter, at the cost of processing time, can be chosen for a better amplitude response. Other types of filters have not been evaluated and may prove valuable.

Controller
The controller has been tuned manually by means of trial-and-error. Computer simulations can be performed to find optimum values for the P, I, and D factors. However, the plant's transfer function must then be identified.

Software
The control module's software has been written in the Arduino IDE. The Arduino IDE provides a higher level of software development such that it is less complicated to interface with the hardware. However, it comes at the cost of processing time. By programming the Arduino processor (Atmel SAM3X8E ARM Cortex-M3) directly, using C, redundant processes can be eliminated which allows for additional processing time for, for example, a higher order digital filter or a higher sampling rate.

Sampling rate
Noise generated by power outlets, is one of the dominant noise source on the measurement data. The Dutch power outlet's provide 230 VAC @ 50 Hz, which coincides with the Nyquist frequency of the sampling rate: 100 Hz. Reducing the sampling rate, in combination with a low pass filter, will remove the noise more efficiently. Increasing the sampling rate prevents aliasing of the power outlet's noise, and allows for a specific band-stop filter around 50 Hz. Furthermore, the higher sampling rate will increase the response time of the system.

Shielding
Noise is generated by external sources, the internal power supplies/transformers, or the motor controller. The control module's case is grounded and should block external sources. However, the sensor wires are unshielded and, though decoupled by optocouplers, can still pass on noise collected and reduce the Signal-to-Noise Ratio. Furthermore, the unshielded transformer, which transforms the 230VAC input to 22VAC, and subsequently transformed to DC power for the Arduino, radiates noise inside the shielded case which can be picked up by sensitive measurement circuits. The relatively low currents make it a less significant noise source than the motor controller. The motor controller switches the high-current signal, up to 8A, at a frequency of 1kHz potentially making the self-induced EMF a dominant noise source. Specifically shielding these components may prove valuable.

Chamber seal
The first phase myocardial chamber design did not incorporate a seal and had to be glued to ensure the chamber did not leak. The second phase myocardial chamber incorporates a printed seal, but had right angles which was likely the reason that the second phase design leaked. A new design had been made, but has not yet been printed. The redesign has rounded angles to ensure the water pressure distributes evenly along the seal; preventing leaks. If the new design does not prevent leaks, the seal design should be re-evaluated.

Water trap / anti-siphon valves
The flow set-up contains two anti-siphon valves to prevent siphonage of the phantom between experiments. In the phase 2 experiments, it had become apparent that the phantom is still being siphoned. A valve can be closed at the end of the aorta. However, the myocardial output does not have a shut-down valve. Adding a myocardial valve will prevent siphonage between experiments if it is closed quickly after shutting down the pump.

An alternative is to add a water trap. A simple elevation has been incorporated to prevent siphonage but it is not a proper water trap. Implementing a water trap should eliminate the siphonage problem completely, assuming the phantom is below the water level in the water trap.

Physical size
The physical size of the phantom is slightly larger than the heart of an average adult. Initially, the dimensions had been forced by mechanical connections. However, the phase 2 design no longer has these restriction, the size has been reduced but not at all possible points. The height of the myocardial chamber can be reduced to 8 millimetres, which is a more typical myocardium wall thickness. The outer diameter of the phantom should not be modified, i.e. the outer walls become thicker, while the chamber becomes smaller. The insert of the myocardial cap, where the O-ring is placed, can be made longer, i.e. inserts deeper into the left ventricle, to further reduce the phase 2 ventricle's volume.

8.2 Trapping

In a true 2-compartment model, the tracer is trapped inside the myocardium. In clinical practice, the tracer is absorbed by the myocardium in the human heart. However, the phantom delays the tracer rather than trapping it. A discussion with Inorganic Membranes group of the University of Twente revealed that the best option is to use Activated Carbon pellets as tissue-mimicking material, combined with a sieve to prevent the pellets from blocking the in- and/or outputs. If the tracer is trapped in the entire chamber, the problems caused by the accumulation of tracer in the apex will have been solved. In addition, the phantom's image in 4DM will be more equivalent to clinical practice.

8.3 Myocardial pumps

The current set-up uses the ratio between pressure drops over the regulator valves to realise the flow to the myocardial chambers. However, slight fluctuations in the primary flow (the cardiac output), will have greater impact on the myocardial chambers since they are not controlled. Assigning a smaller pump, one for each myocardial chamber, a flow-feedback loop can be made to precisely control the myocardial flow. The phase 2 myocardial chamber's output already converges to a single output which can be directly connected to a pump. However, it will require an additional motor controller to allow for three extra pumps. The current motor controller can support only 2 pumps. Three extra pumps will introduce more noise inside the control module and extra precautions should then be taken to prevent further interference on the measurements, see section 8.1 (shielding).

Bibliography

Anderson, J., Ackerman, J., and Garbow, J. (2011). Semipermeable hollow fiber phantoms for development and validation of perfusion-sensitive mr methods and signal models. *Concepts in Magnetic Resonance Part B: Magnetic Resonance Engineering*, 39(3):149–158.

Boese, A., Gugel, S., Serowy, S., Purmann, J., Rose, G., Beuing, O., Skalej, M., Kyriakou, Y., and Deuerling-Zheng, Y. (2013). Performance evaluation of a C-Arm CT perfusion phantom. *International journal of computer assisted radiology and surgery*, 8(5):799–807.

Carson, R. E. (2005). Tracer kinetic modeling in PET. In *Positron Emission Tomography*, pages 127–159. Springer.

Chiribiri, A., Schuster, A., Ishida, M., Hautvast, G., Zarinabad, N., Morton, G., Otton, J., Plein, S., Breeuwer, M., Batchelor, P., et al. (2013). Perfusion phantom: An efficient and reproducible method to simulate myocardial first-pass perfusion measurements with cardiovascular magnetic resonance. *Magnetic Resonance in medicine*, 69(3):698–707.

Driscoll, B., Keller, H., and Coolens, C. (2011). Development of a dynamic flow imaging phantom for dynamic contrast-enhanced CT. *Medical physics*, 38(8):4866–4880.

Ebrahimi, B., Swanson, S. D., and Chupp, T. E. (2010). A microfabricated phantom for quantitative MR perfusion measurements: validation of singular value decomposition deconvolution method. *IEEE transactions on Biomedical Engineering*, 57(11):2730–2736.

Erlandsson, K., Kacperski, K., Van Gramberg, D., and Hutton, B. F. (2009). Performance evaluation of D-SPECT: a novel SPECT system for nuclear cardiology. *Physics in Medicine & Biology*, 54(9):2635.

Gambhir, S. S., Berman, D. S., Ziffer, J., Nagler, M., Sandler, M., Patton, J., Hutton, B., Sharir, T., Haim, S. B., and Haim, S. B. (2009). A novel high-sensitivity rapid-acquisition single-photon cardiac imaging camera. *Journal of Nuclear Medicine*, 50(4):635–643.

Ganguly, A., Fieselmann, A., Boese, J., Rohkohl, C., Hornegger, J., and Fahrig, R. (2012). In vitro evaluation of the imaging accuracy of C-arm conebeam CT in cerebral perfusion imaging. *Medical physics*, 39(11):6652–6659.

Goshen, E., Beilin, L., Stern, E., Kenig, T., Goldkorn, R., and Ben-Haim, S. (2018). Feasibility study of a novel general purpose CZT-based digital SPECT camera: initial clinical results. *EJNMMI physics*, 5(1):6.

Hashimoto, H., Suzuki, K., Okaniwa, E., Iimura, H., Abe, K., and Sakai, S. (2018). The effect of scan interval and bolus length on the quantitative accuracy of cerebral computed tomography perfusion analysis using a hollow-fiber phantom. *Radiological physics and technology*, 11(1):13–19.

Khalil, M. M., Tremoleda, J. L., Bayomy, T. B., and Gsell, W. (2011). Molecular SPECT imaging: an overview. *International journal of molecular imaging*, 2011.

Kim, M., Abbey, C. K., and Insana, M. F. (2016). Efficiency of US tissue perfusion estimators. *IEEE transactions on ultrasonics, ferroelectrics, and frequency control*, 63(8):1131–1139.

Klotz, E. and König, M. (1999). Perfusion measurements of the brain: using dynamic CT for the quantitative assessment of cerebral ischemia in acute stroke. *European journal of radiology*, 30(3):170–184.

Kumar, A. (2016). Comparison of Different Types of IIR Filters. *International Journal of Advanced Research in Electronics and Communication Engineering*, 5(2):10.

Lin, F. Y., Devereux, R. B., Roman, M. J., Meng, J., Jow, V. M., Jacobs, A., Weinsaft, J. W., Shaw, L. J., Berman, D. S., Callister, T. Q., et al. (2008). Cardiac chamber volumes, function, and mass as determined by 64-multidetector row computed tomography: mean values among healthy adults free of hypertension and obesity. *JACC: Cardiovascular Imaging*, 1(6):782–786.

Lohmaier, S., Ghanem, A., Veltmann, C., Sommer, T., Bruce, M., and Tiemann, K. (2004). In vitro and in vivo studies on continuous echo-contrast application strategies using SonoVue in a newly developed rotating pump setup. *Ultrasound in medicine & biology*, 30(9):1145–1151.

Maceira, A., Prasad, S., Khan, M., and Pennell, D. (2006). Normalized left ventricular systolic and diastolic function by steady state free precession cardiovascular magnetic resonance. *Journal of Cardiovascular Magnetic Resonance*, 8(3):417–426.

Mathys, C., Rybacki, K., Wittsack, H.-J., Lanzman, R. S., Miese, F. R., Macht, S., Eicker, S., zu Hörste, G. M., Antoch, G., and Turowski, B. (2012). A phantom approach to interscanner comparability of computed tomographic brain perfusion parameters. *Journal of computer assisted tomography*, 36(6):732–738.

Mehta, P. K., Wei, J., and Wenger, N. K. (2015). Ischemic heart disease in women: a focus on risk factors. *Trends in cardiovascular medicine*, 25(2):140–151.

Mendis, S., Puska, P., Norrving, B., Organization, W. H., et al. (2011). *Global atlas on cardiovascular disease prevention and control*. Geneva: World Health Organization.

Noguchi, T., Yoshiura, T., Hiwatashi, A., Togao, O., Yamashita, K., Kobayashi, K., Mihara, F., and Honda, H. (2007). Quantitative perfusion imaging with pulsed arterial spin labeling: a phantom study. *Magnetic Resonance in Medical Sciences*, 6(2):91–97.

O'Doherty, J., Chalampalakis, Z., Schleyer, P., Nazir, M. S., Chiribiri, A., and Marsden, P. K. (2017). The effect of high count rates on cardiac perfusion quantification in a simultaneous PET-MR system using a cardiac perfusion phantom. *EJNMMI physics*, 4(1):31.

Osborne, L. F., Brummond, J., Hart, R., Zarean, M., Conger, S. M., et al. (2005). Clarus: Concept of operations. Technical report, United States. Federal Highway Administration.

Otton, J., Morton, G., Schuster, A., Bigalke, B., Marano, R., Olivotti, L., Nagel, E., and Chiribiri, A. (2013). A direct comparison of the sensitivity of CT and MR cardiac perfusion using a myocardial perfusion phantom. *Journal of cardiovascular computed tomography*, 7(2):117–124.

Pelgrim, G., Handayani, A., Dijkstra, H., Prakken, N., Slart, R., Oudkerk, M., Van Ooijen, P., Vliegenthart, R., and Sijens, P. (2016). Quantitative myocardial perfusion with dynamic contrast-enhanced imaging in MRI and CT: theoretical models and current implementation. *BioMed research international*, 2016.

Rook, P. (1986). Controlling software projects. *Software Engineering Journal*, 1(1):7–16.

Sakano, R., Kamishima, T., Nishida, M., and Horie, T. (2015). Power Doppler signal calibration between ultrasound machines by use of a capillary-flow phantom for pannus vascularity in rheumatoid finger joints: a basic study. *Radiological physics and technology*, 8(1):120–124.

Suzuki, K., Hashimoto, H., Okaniwa, E., Iimura, H., Suzaki, S., Abe, K., and Sakai, S. (2017). Quantitative accuracy of computed tomography perfusion under low-dose conditions, measured using a hollow-fiber phantom. *Japanese journal of radiology*, 35(7):373–380.

Teslow, T. and Robb, R. (1991). X-ray computed tomographic (CT) phantom designed for the development of techniques for measurement of myocardial perfusion. *Physics in Medicine & Biology*, 36(10):1407.

Vaartjes, I., Van Dis, I., Visseren, F., Bots, M., et al. (2013). Hart-en vaatziekten in Nederland 2013, cijfers over leefstijl, risicofactoren, ziekte en sterfte. *Den Haag: Hartstichting*, pages 2941–2947.

Veltmann, C., Lohmaier, S., Schlosser, T., Shai, S., Ehlgen, A., Pohl, C., Becher, H., and Tiemann, K. (2002). On the design of a capillary flow phantom for the evaluation of ultrasound contrast agents at very low flow velocities. *Ultrasound in medicine & biology*, 28(5):625–634.

Wagenaar, D. J. (2004). CdTe and CdZnTe semiconductor detectors for nuclear medicine imaging. In *Emission Tomography*, pages 269–291. Elsevier.

Wang, Y., Kim, S.-E., DiBella, E. V., and Parker, D. L. (2010). Flow measurement in MRI using arterial spin labeling with cumulative readout pulses—theory and validation. *Medical physics*, 37(11):5801–5810.

Yoneyama, H., Shibutani, T., Konishi, T., Mizutani, A., Hashimoto, R., Onoguchi, M., Okuda, K., Matsuo, S., Nakajima, K., and Kinuya, S. (2017). Validation of Left Ventricular Ejection Fraction with the IQ• SPECT System in Small-Heart Patients. *Journal of nuclear medicine technology*, 45(3):201–207.